

# Quantitative spectroscopy of B-type supergiants

D. Weißmayer<sup>1</sup>, N. Przybilla<sup>1</sup>, and K. Butler<sup>2</sup>

<sup>1</sup> Institut für Astro- und Teilchenphysik, Universität Innsbruck, Technikerstr. 25/8, 6020 Innsbruck, Austria  
e-mail: david.wessmayer@uibk.ac.at ; norbert.przybilla@uibk.ac.at

<sup>2</sup> LMU München, Universitätssternwarte, Scheinerstr. 1, 81679 München, Germany

Received ; accepted

## ABSTRACT

**Context.** B-type supergiants are versatile tools to address a number of highly-relevant astrophysical topics, ranging from stellar atmospheres over stellar and galactic evolution to the characterisation of interstellar sightlines and to the cosmic distance scale.

**Aims.** A hybrid non-LTE (local thermodynamic equilibrium) approach – involving line-blanketed model atmospheres computed under the assumption of LTE in combination with line formation calculations that account for deviations from LTE – is tested for quantitative analyses of B-type supergiants of mass up to about  $30 M_{\odot}$ , characterising a sample of 14 Galactic objects in a comprehensive way.

**Methods.** Hydrostatic plane-parallel atmospheric structures and synthetic spectra computed with Kurucz's ATLAS12 code together with the non-LTE line-formation codes DETAIL/SURFACE are compared to results from full non-LTE calculations with TLUSTY, and the effects of turbulent pressure on the models are investigated. High-resolution spectra at signal-to-noise ratio  $> 130$  are analysed for atmospheric parameters, using Stark-broadened hydrogen lines and multiple metal ionisation equilibria, and for elemental abundances. Fundamental stellar parameters are derived by considering stellar evolution tracks and Gaia early data release 3 (EDR3) parallaxes. Interstellar reddening and the reddening law along the sight lines towards the target stars are determined by matching model spectral energy distributions to observed ones.

**Results.** Our hybrid non-LTE approach turns out to be equivalent to hydrostatic full non-LTE modelling for the deeper photospheric layers of the B-type supergiants under consideration, where most lines of the optical spectrum are formed. Turbulent pressure can become relevant for microturbulent velocities larger than  $10 \text{ km s}^{-1}$ . The changes in the atmospheric density structure affect many diagnostic lines, implying systematic changes in atmospheric parameters, for instance an increase in surface gravities by up to 0.05 dex. A high precision and accuracy is achieved for all derived parameters by bringing multiple indicators to agreement simultaneously. Effective temperatures are determined to 2-3% uncertainty, surface gravities to better than 0.07 dex, masses to about 5%, radii to about 10%, luminosities to better than 25%, and spectroscopic distances to 10% uncertainty typically. Abundances for chemical species that are accessible from the optical spectra (He, C, N, O, Ne, Mg, Al, Si, S, Ar, and Fe) are derived with uncertainties of 0.05 to 0.10 dex ( $1\sigma$  standard deviations). The observed spectra are reproduced well by the model spectra. The derived N/C versus N/O ratios tightly follow the predictions from Geneva stellar evolution models that account for rotation, and spectroscopic and Gaia EDR3 distances are closely matched. Finally, the methodology is tested for analyses of intermediate-resolution spectra of extragalactic B-type supergiants.

**Key words.** Stars: abundances – Stars: atmospheres – Stars: early-type – Stars: evolution – Stars: fundamental parameters – supergiants

## 1. Introduction

Massive stars are drivers of the evolution of galaxies as they are crucial contributors to the energy and momentum budget of the interstellar medium (ISM), and they are sources of nucleosynthesis products (e.g. [Matteucci 2008](#)). This is because of their ionising radiation, their strong stellar winds, and final fate in supernova explosions and – under certain circumstances – as  $\gamma$ -ray bursts. Multiple facets of the evolution of single and binary massive stars are largely understood, though many details have yet to be resolved (e.g. [Maeder & Meynet 2012](#); [Langer 2012](#); [Sana et al. 2012](#)), with several independent grids of evolutionary models being available (e.g. [Brott et al. 2011](#); [Ekström et al. 2012](#); [Limongi & Chieffi 2018](#); [Szécsi et al. 2022](#)). Improvements in our understanding of galactic and massive star evolution are driven by observational constraints, either qualitatively by consideration of new aspects, or quantitatively by a reduction in observational uncertainties (which is of interest here).

The evolution of massive stars in the upper Hertzsprung-Russell diagram (HRD) splits overall into two domains, connected to the Humphreys-Davidson limit ([Humphreys & Davidson 1979](#)).

Stars more massive than  $\sim 40 M_{\odot}$  remain blue objects throughout their entire life because strong stellar winds and probably pulsational instabilities lead to the loss of their envelopes. These early and mid-O dwarfs and giants on the main sequence (MS) evolve into early B-type hypergiants (e.g. [Clark et al. 2012](#); [Herrero et al. 2022](#)) and supergiants of luminosity class Ia, which constitute one of the more frequently populated regions of post-MS evolution in the HRD (e.g. [Castro et al. 2014](#)). In this evolutionary stage, they belong to the visually brightest stars in star-forming galaxies in addition to their high energy output at UV wavelengths and they are likely to become luminous blue variables (LBVs) at more advanced evolutionary stages, and finally Wolf-Rayet (WR) stars. Realistic quantitative spectroscopy of these objects requires hydrodynamical stellar atmosphere models that account for deviations from local thermodynamic equilibrium (non-LTE) and metal-line blanketing ([Hillier & Miller 1998](#); [Pauldrach et al. 2001](#); [Gräfener et al. 2002](#); [Puls et al. 2005](#)).

The less massive stars (i.e.  $M \lesssim 30 M_{\odot}$ ) with bolometric magnitudes larger than about  $-9.5$  to  $-10$  mag evolve into red supergiants (RSGs) with extended hydrogen-rich envelopes at least

once during their lifetime. They become B-type supergiants of luminosity classes Ib and Iab and at the lower limit of the massive star regime at  $\sim 8\text{--}9 M_{\odot}$  also bright giants (luminosity class II) when they evolve from late-O and early-B dwarfs on the MS on their way towards the RSG stage. Alternatively, some B-type supergiants may be post-RSG objects like Sk  $-69^{\circ}$  202, the precursor of SN 1987A (West et al. 1987), with possible evolutionary channels provided by binary (Podsiadlowski 1992) as well as single star evolution (Hirschi et al. 2004). Such objects should be rare. While signatures of mass-loss are still present in the spectra of these lower-luminosity B-type supergiants, in the optical part of the spectrum they are restricted to a few spectral lines like H $\alpha$ . The photospheric spectrum on the other hand is formed under conditions close to hydrostatic equilibrium, so that hydrostatic line-blanketed non-LTE model atmospheres (Hubeny & Lanz 1995) may be employed for their quantitative analysis. This was confirmed by a comparison of hydrostatic and hydrodynamic non-LTE model atmospheres for luminous early B-type supergiants by Dufton et al. (2005).

Galactic B-type supergiants have been investigated for a long time, starting with the early work on the B1 Ib star  $\zeta$  Per by Cayrel (1958) based on photographic plate spectra and the studies of Dufton (1972, 1979) using improved LTE model atmospheres. The advent of spectroscopy with CCD detectors facilitated the first spectral atlas of Galactic B-type supergiants to be obtained at optical wavelengths and spectral line behaviours to be investigated qualitatively over the entire spectral type (Lennon et al. 1992, 1993). This dataset was later employed for the first larger-scale investigation of atmospheric parameters and the chemical abundances of B-type supergiants, employing plane-parallel and hydrostatic non-LTE atmospheres composed of hydrogen and helium, plus subsequent line-formation computations for the metals (McErlean et al. 1999). A main focus were abundances of carbon, nitrogen, and oxygen as tracers for the presence of CN(O)-processed material in the atmospheres, modified from initial standard values due to evolutionary processes. The Lennon et al. spectra were also utilised to derive stellar wind parameters for Galactic B-type supergiants by Kudritzki et al. (1999) to constrain the wind momentum-luminosity relationship (Puls et al. 1996) for distance measurements of this kind of object, employing hydrodynamical H+He model atmospheres in non-LTE. About the same time some B-type supergiants were employed in the derivation of Galactic abundance gradients, using a differential pure LTE analysis (Smartt et al. 2001b).

Studies with sophisticated line-blanketed non-LTE model atmospheres followed, concentrating on the derivation of atmospheric, stellar wind, and fundamental parameters, often employing observational data of higher resolving power and wider wavelength coverage than in the earlier work (Crowther et al. 2006; Lefever et al. 2007; Markova & Puls 2008; Searle et al. 2008; Haucke et al. 2018). Elemental abundances were discussed in some of these works, focusing again on carbon, nitrogen, and oxygen as tracers for mixing of the atmospheric layers with nuclear-processed material from the stellar core. Models predict very tight correlations for the surface CNO abundances independent of single or binary star evolution (Przybilla et al. 2010; Maeder et al. 2014). More comprehensive chemical information (C, N, O, Mg, and Si) was derived by use of line-blanketed hydrostatic non-LTE model atmospheres for B-type supergiants in Galactic open clusters by Hunter et al. (2009), while Fraser et al. (2010) studied atmospheric parameters, nitrogen abundances, and rotational and macroturbulent velocities based on high-resolution spectra. Similar work with an extended observational database was later conducted by Simón-Díaz et al.

(2017). On the cool end of the B-type supergiants and towards the early A-type supergiants a sample of objects was analysed by Firnstein & Przybilla (2012), using techniques very similar to those employed in the present work (Przybilla et al. 2006a).

The enormous luminosities of B-type supergiants makes their spectroscopy feasible at distances beyond the Milky Way. Objects in the Magellanic Clouds were therefore intensely studied, concentrating initially on the more metal-poor Small Magellanic Cloud (SMC, Trundle et al. 2004; Lee et al. 2005; Dufton et al. 2005), where surface enrichments with nuclear-processed matter due to rotational mixing were predicted to be stronger (e.g. Maeder & Meynet 2001; Georgy et al. 2013). Only later was attention turned towards the Large Magellanic Cloud (LMC, Hunter et al. 2009; McEvoy et al. 2015; Urbaneja et al. 2017).

Even earlier, first studies of B-type supergiants were undertaken for more distant galaxies of the Local Group, based on intermediate-resolution spectra and aiming at the determination of stellar parameters and elemental abundances. Work on M31, based on the McErlean et al. (1999) approach or LTE techniques (Smartt et al. 2001a; Trundle et al. 2002) and on NGC6822 (Muschielok et al. 1999) was followed by studies of M33 supergiants using hydrodynamical non-LTE atmospheres (Urbaneja et al. 2005b; U et al. 2009), aiming at the derivation of abundance and metallicity gradients, and distances. Metallicities and distances (derived via application of the Flux-weighted Gravity-Luminosity Relationship, FGLR, Kudritzki et al. 2003, 2008) were also the focus of studies of the Local Group dwarf irregular galaxies IC1613 (Bresolin et al. 2007; Berger et al. 2018) and WLM (Bresolin et al. 2006; Urbaneja et al. 2008).

B-type supergiants in galaxies beyond the Local Group have also been studied, investigating not only stellar parameters, metallicities and metallicity gradients, but also interstellar reddening in these galaxies, distances, and the galaxy mass-metallicity relationship (e.g. Lequeux et al. 1979; Tremonti et al. 2004; Maiolino et al. 2008), which is a key to the study of galaxy evolution. Objects in NGC300 (Bresolin et al. 2002, 2004; Urbaneja et al. 2003, 2005a) and NGC55 (Castro et al. 2012; Kudritzki et al. 2016) in the Sculptor filament of galaxies were investigated, and in NGC3109 (Evans et al. 2007; Hosek et al. 2014), a member of the nearby Antlia-Sextans group. At even larger distances of about 3.5, 4.5, and 6.5 Mpc, respectively, B-type supergiants were analysed in the grand design spiral galaxy M81 (Kudritzki et al. 2012), in the barred spiral galaxy M83 (Bresolin et al. 2016), and in the field spiral galaxy NGC3621 (Kudritzki et al. 2014), all based on spectra obtained with 8-10 m-class telescopes.

In addition to their usefulness for stellar studies, B-type supergiants are frequently employed as background stars for studies of diffuse interstellar bands (DIBs) because they facilitate sight lines to be covered to large distances and provide continuous spectra with relatively few intrinsic stellar spectral features. B-type supergiants are therefore not only employed to cover interstellar sight lines in the Milky Way (e.g. Cox et al. 2017; Ebenbichler et al. 2022), but also as tracers of DIBs in other galaxies such as the Magellanic Clouds (Cox et al. 2006, 2007) and M31 (Cordiner et al. 2008, 2011).

Overall, B-type supergiants show enormous potential as versatile tools to address multiple astrophysical topics of high relevance. The present paper addresses the quantitative spectroscopy of B-type supergiants based on a hybrid non-LTE approach – combining hydrostatic line-blanketed LTE atmospheres with subsequent non-LTE line formation –, applying state-of-the-art model atoms. The paper is organised as follows: observations and the data reduction are summarised in Sect. 2. The hybrid

**Table 1.** B-type supergiant sample.

ID#	Object	Sp. T. <sup>a</sup>	Sp. T. <sup>b</sup>	OB Assoc. <sup>c</sup>	$V^d$ mag	$B - V^d$ mag	$U - B^d$ mag	Date of Obs. YYYY-MM-DD	$T_{\text{exp}}$ s	$S/N$
FOCES $R = 40\,000$										
1	HD 7902	B6 Ib	B6 Ia	NGC 457	6.988±0.023	0.414±0.009	-0.380±0.004	2001-09-27	896	320
2	HD 14818	B2 Ia	B2 Ia	Per OB1	6.253±0.016	0.301±0.007	-0.613±0.009	2005-09-22	3×1200	320
3	HD 25914	B5 Ia	B6 Ia	Cam OB3	7.99	0.6	-0.28	2005-09-25	2700	180
4	HD 36371	B4 Ib	B5 Ia	Aur OB1	4.766±0.014	0.345±0.013	-0.445±0.015	2001-09-30	240	480
5	HD 183143	B6 Ia	B7 Ia <sup>e</sup>	Field	6.839±0.017	1.185±0.018	0.165±0.031	2001-09-25	900	220
6	HD 184943	B8 Ia/Iab	B8 Iab	Vul OB1	8.184±0.016	0.725±0.009	-0.073±0.011	2005-09-25	1800	130
7	HD 191243	B6 Ib	B5 Ib	Cyg OB3	6.111±0.022	0.151±0.014	-0.447±0.034	2005-09-21	900	350
8	HD 199478	B8 Ia	B8 Ia	NGC 6991	5.679±0.018	0.461±0.017	-0.341±0.028	2001-09-26	1200 + 3×600	240
FEROS $R = 48\,000$										
9	HD 51309	B3 Ib/II	B3 Ib <sup>f</sup>	Field	4.380±0.014	-0.064±0.008	-0.704±0.018	2011-12-09	2×45	440
10	HD 111990	B1/B2 Ib	B2 Iab	Cen OB1	6.792±0.015	0.242±0.006	-0.579±0.008	2013-08-17	300	260
11	HD 119646	B1 Ib/II	B1.5 Ib	Field	6.602±0.020	0.118±0.007	-0.685±0.022	2005-04-23	400 + 410	490
12	HD 125288	B5 Ib/II	B5 II	Field	4.336±0.013	0.115±0.007	-0.444±0.007	2013-08-20	240	410
13	HD 159110	B4 Ib	B2 II	Field	7.578±0.009	-0.022±0.010	-0.685±0.012	2005-04-23	2×1000	410
14	HD 164353	B5 I/Ib	B5 Ib <sup>e</sup>	Coll 359	3.961±0.019	0.023±0.012	-0.606±0.019	2013-08-20	135 + 180	540

**Notes.** <sup>(a)</sup> adopted from SIMBAD <sup>(b)</sup> this work <sup>(c)</sup> Humphreys (1978) <sup>(d)</sup> Mermilliod (1997) <sup>(e)</sup> Gray & Corbally (2009) <sup>(f)</sup> Walborn's B-type standards (Gray & Corbally 2009)

non-LTE modelling approach is introduced and comparisons to full non-LTE model atmospheres are made in Sect. 3. Then, details of the analysis methodology are discussed in Sect. 4. Section 5 presents all results from the B-type supergiant sample analysis and the suitability of the method for quantitative analyses at intermediate spectral resolution is investigated in Sect. 6, in preparation for extragalactic studies applying the hybrid non-LTE approach. Conclusions are drawn in Sect. 7. An example of a detailed comparison of a tailored model with an observed spectrum is given in Appendix A.

## 2. Observations and data reduction

High-resolution spectra of 14 Galactic B-type supergiants at high signal-to-noise ratio  $S/N$  constitute the observational basis for the present work. The spectral range B1.5 to B8 at luminosity classes II, Ib, Iab, and Ia is covered, extending previous work on late B and early A-type supergiants of similar masses and luminosities (Przybilla et al. 2006a; Schiller & Przybilla 2008; Farnstein & Przybilla 2012) towards higher temperatures. Basic information on the star sample and the observing log are summarised in Table 1. An internal ID number is given, the Henry-Draper catalogue designation, the spectral type, and an OB association or open cluster membership is indicated. Spectral type information from the SIMBAD database<sup>1</sup> is summarised, as well as from a re-determination in the present work, based on anchor points of the Morgan-Keenan system and Walborn's B-type standards (Gray & Corbally 2009). The luminosity class determination was based on Balmer line appearance, in particular concentrating on  $H\alpha$ . Moreover, photometric data in the Johnson system are given in Table 1, the  $V$  magnitude and the  $B - V$  and  $U - B$  colours. The observing log provides the date of observation, exposure times, and the  $S/N$  of the final spectrum, measured around 5585 Å.

The raw spectra were obtained with two instruments. Objects in the northern hemisphere were observed with the Fibre Optics Echelle Cassegrain Spectrograph (FOCES, Pfeiffer et al. 1998) on the Calar Alto 2.2 m telescope in two observing runs in 2001

and 2005. The spectra cover a wavelength range from 3860 to 9580 Å at a resolving power  $R = \lambda/\Delta\lambda \approx 40\,000$ , with 2 pixels covering a  $\Delta\lambda$  resolution element. A median filter was applied to the raw images to remove effects of bad pixels and cosmetics in an initial step. Then, the FOCES semi-automatic pipeline (Pfeiffer et al. 1998) was employed for the data reduction, performing subtraction of bias and dark current, flatfielding, wavelength calibration using Th-Ar exposures, and rectification and merging of the echelle orders. A major advantage of the FOCES design was that the order tilt was much more homogeneous than in similar spectrographs. This facilitated a more robust continuum rectification than is usually feasible, even in the case of broad features like the hydrogen Balmer lines, which can span more than one echelle order (for a discussion see Korn 2002). Two objects had multiple exposures taken consecutively that were combined to increase the  $S/N$  of the final spectrum.

Objects of the southern hemisphere were observed with the Fiberfed Extended Range Optical Spectrograph (FEROS, Kaufer et al. 1999) on the European Southern Observatory (ESO)/Max-Planck Society 2.2 m telescope in La Silla, Chile. FEROS provides a resolving power of  $R \approx 48\,000$ , with a 2.2-pixel resolution element. The reduced Phase 3 spectra were downloaded from the ESO Science Portal<sup>2</sup>. Continuum normalisation was achieved by division by a spline function to carefully selected continuum windows. Only the  $\sim 3800$  to  $9000$  Å range of the full wavelength coverage of FEROS satisfied our quality criteria for the quantitative analysis.

Examples of the analysed spectra can be seen in Fig. 1, to demonstrate the data quality achieved for the present work. The figure focuses on three diagnostic wavelength regions: the window around  $H\delta$  with Si II and Si IV lines plus several He I and O II lines, among others, the region of the Si III triplet plus numerous O II lines and on the wind-affected  $H\alpha$  line with the adjacent strong C II doublet. We note how the density of spectral lines increases towards the earlier spectral types. We also note that objects at luminosity class Ib show nearly symmetric  $H\alpha$  absorption, that is a negligible stellar wind, while the wind gives

<sup>1</sup> <http://simbad.u-strasbg.fr/simbad/sim-fid>

<sup>2</sup> <https://archive.eso.org/scienceportal/home>



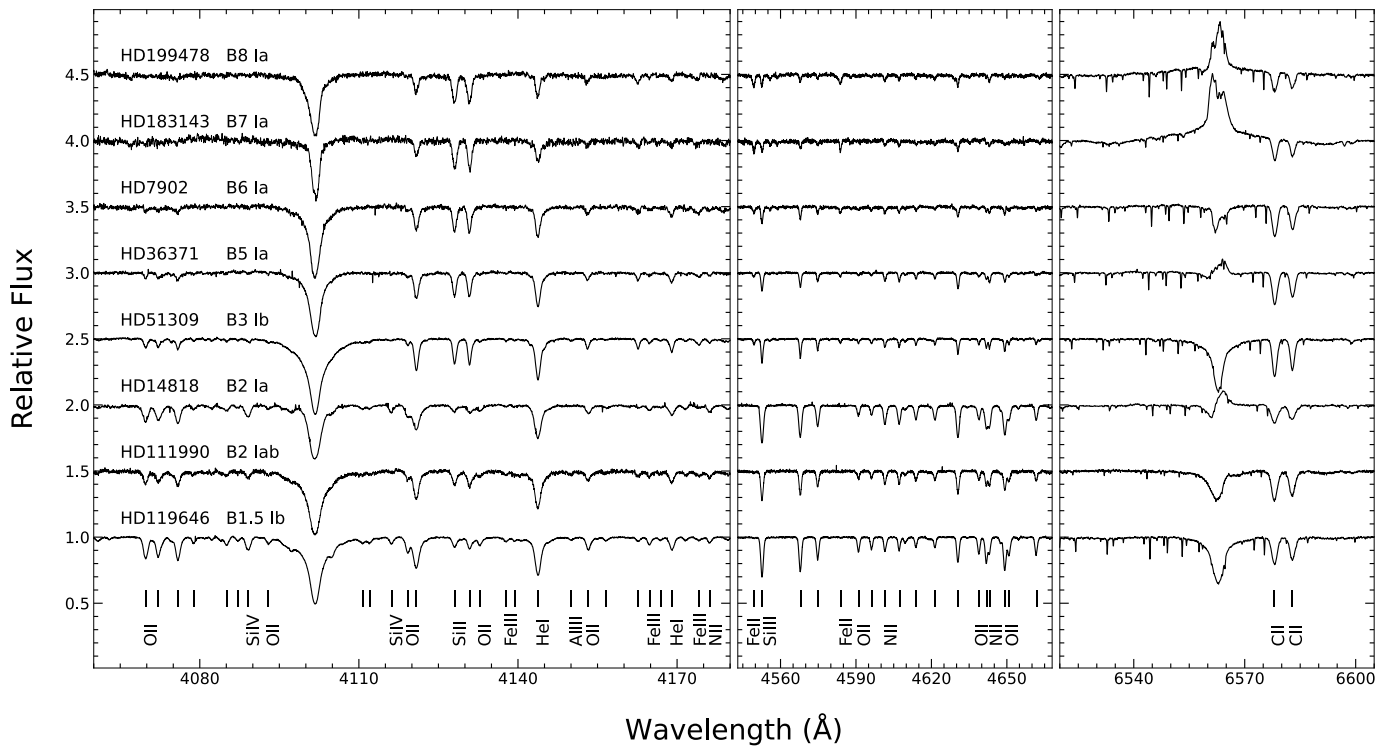


**Fig. 1.** Subset of the analysed spectra ordered with respect to spectral type. The three panels showcase spectral windows with prominent features in the spectra of B-type supergiants, see the text for a discussion.

**Table 2.** IUE spectrophotometry used in the present work.

ID #	Object	SW	Date	LW	Date
2	HD14818	P18658	1982-11-26	R14722	1982-11-26
5	HD183143	P06550	1979-09-18	R05637	1979-09-20
8	HD199478	P07596	1980-01-07	R06573	1980-01-07
9	HD51309	P13936	1981-05-09	R10551	1981-05-09
10	HD111990	...	...	P13362	1988-06-05
12	HD125288	P19460	1983-03-14	R15489	1983-03-14
13	HD159110	P45210	1992-07-22	P21218	1991-09-11
14	HD164353	P10172	1980-09-18	R08836	1980-09-18

rise to pronounced  $H\alpha$  emission at luminosity class Ia, while  $H\delta$  is essentially symmetric at the luminosities covered here.

Besides the optical spectra, additional archival photometric data and UV spectrophotometry were collected to establish the objects' spectral energy distributions (SEDs). For all analysed objects, optical photometry in the Johnson  $U$ ,  $B$ , and  $V$  bands by [Mermilliod \(1997\)](#) was adopted,  $J$ ,  $H$ , and  $K$  magnitudes from the Two Micron All Sky Survey (2MASS, [Skrutskie et al. 2006](#)) and  $W1$  to  $W4$  IR-photometric data from the Wide-field Infrared Survey Explorer (WISE) mission, from the ALLWISE data release ([Cutri et al. 2021](#)). For a thorough comparison in the ultraviolet wavelength range, spectrophotometry taken by the International Ultraviolet Explorer (IUE) were preferred in our analysis. The designation and observation date for each IUE-spectrum used in the analysis are given in Table 2. For both short-wavelength (SW,  $\lambda\lambda 1150$ – $1978$  Å) and long-wavelength data (LW,  $\lambda\lambda 1851$ – $3347$  Å) low-resolution spectrophotometry taken with the large aperture was favoured; in cases where only high-resolution data were available, the spectra were artificially degraded in resolution for the analysis. Whenever possible, SW and LW data observed close in time were employed.

For several of the stars of our sample, IUE data was either unavailable or inconsistent with the optical and infrared photometry (possibly because of a misalignment of the aperture). In these cases photometric measurements by the Astronomical Netherlands Satellite (ANS, [Wesselius et al. 1982](#)) or from the Belgian/UK Ultraviolet Sky Survey Telescope (S2/68, [Thompson et al. 1995](#)) on board the European Space Research Organisation (ESRO) TD1 satellite were used.

### 3. Model atmospheres and spectrum synthesis

Our methodology for the analysis of B-type supergiants is based on a hybrid non-LTE approach of calculating static, plane-parallel line-blanketed LTE model atmospheres, which serve as the basis of non-LTE line formation computations. The basic approach was outlined by [Przybilla et al. \(2006a\)](#) where its potential to accurately reproduce all relevant spectral features of late B- and early A-type (BA-type) supergiants was shown. This methodology was validated in a direct comparison with full non-LTE hydrodynamic line-blanketed model atmospheres ([Nieva & Simón-Díaz 2011](#)) and was used to derive high-precision atmospheric and fundamental stellar parameters and abundances for many chemical species in early B-type MS stars ([Nieva & Przybilla 2012, 2014; Irrgang et al. 2014](#)). Moreover, the hybrid approach is applicable to analyses of a wide range of other B-type stars, such as subdwarf B-stars ([Przybilla et al. 2006b; Schafferoth et al. 2021](#)), MS Bp ([Przybilla et al. 2008b](#)), He-strong stars ([Przybilla et al. 2016, 2021](#)), and supergiant extreme helium stars ([Kupfer et al. 2017](#)). In the following, we therefore briefly recap the basic principles and the model codes and will concentrate on new aspects relevant for the present work.

**Table 3.** Model atoms for non-LTE calculations with DETAIL.

Ion	Terms	Transitions	Reference
H	20	190	[1]
He I	29+6	162	[2]
C II/III	68/70	425/373	[3]
N I/II	89/77	668/462	[4]
O I/II	51/176+2	243/2559	[5]
Ne I/II	153/78	952/992	[6]
Mg II	37	236	[7]
Al II/III	54+6/46+1	378/272	[8]
Si II/III/IV	52+3/68+4/33+2	357/572/242	[9]
S II/III	78/21	302/34	[10]
Ar II	56	596	[11]
Fe II/III/IV	265/60+46/65+70	2887/2446/2094	[12]

**References.** [1] Przybilla & Butler (2004); [2] Przybilla (2005); [3] Nieva & Przybilla (2006), Nieva & Przybilla (2008); [4] Przybilla & Butler (2001); [5] Przybilla et al. (2000), Przybilla & Butler (in prep.); [6] Morel & Butler (2008); [7] Przybilla et al. (2001a); [8] Przybilla (in prep.); [9] Przybilla & Butler (in prep.); [10] Vrancken et al. (1996), updated; [11] Butler (in prep.); [12] Becker (1998), Morel et al. (2006).

### 3.1. Models and programmes

The LTE line-blanketed model atmospheres used in this work were calculated with the ATLAS12 code (Kurucz 2005), which assumes plane-parallel geometry, a stationary and hydrostatic stratification, and chemical homogeneity. In contrast to the previous version ATLAS9 (Kurucz 1993, which is still required to provide converged starting models) it does not rely on pretabulated opacity distribution functions (ODFs), but evaluates the opacities via opacity sampling (OS). The code thus facilitates model atmospheres to be calculated for freely specified input abundances and microturbulent velocities, including the turbulent pressure in the hydrostatic equation for a self-consistent solution.

The LTE model atmospheres were then used to compute non-LTE level population densities via an updated and extended version of DETAIL (Giddings 1981) by solving the coupled radiative transfer and statistical equilibrium equations adopting an accelerated lambda iteration scheme by Rybicki & Hummer (1991), and considering line blocking based on the Kurucz' OS scheme. State-of-the-art model atoms were employed, as summarised in Table 3. There, for each chemical species the considered ions are listed, the number of explicit terms (+ superlevels) and radiative bound-bound transitions, and references. All model atoms are completed by the ground term of the next higher ionisation stage not indicated here.

While most of the model atoms were used previously in other studies, a new model atom for O II was employed in the present work for the first time. We describe it briefly. Level energies were adopted from Martin et al. (1993) and combined into 176 LS-coupled terms up to principal quantum number  $n = 8$  and the levels for  $n = 9$  combined into two superlevels, one each for the doublet and quartet spin systems. Oscillator strengths and photoionisation cross-sections were for the most part adopted from the Opacity Project (OP, e.g. Seaton et al. 1994), with several improved data taken from Wiese et al. (1996), and supplemented by Kurucz' recently computed oscillator strengths<sup>3</sup> for missing transitions. Electron impact-excitation data for a large number of transitions were available from the ab-initio calculations of Tayal (2007) and Mao et al. (2020). Missing data were provided by use of Van Regemorter's formula (van Regemorter 1962) for radiatively permitted or Allen's formula (Allen 1973) for for-

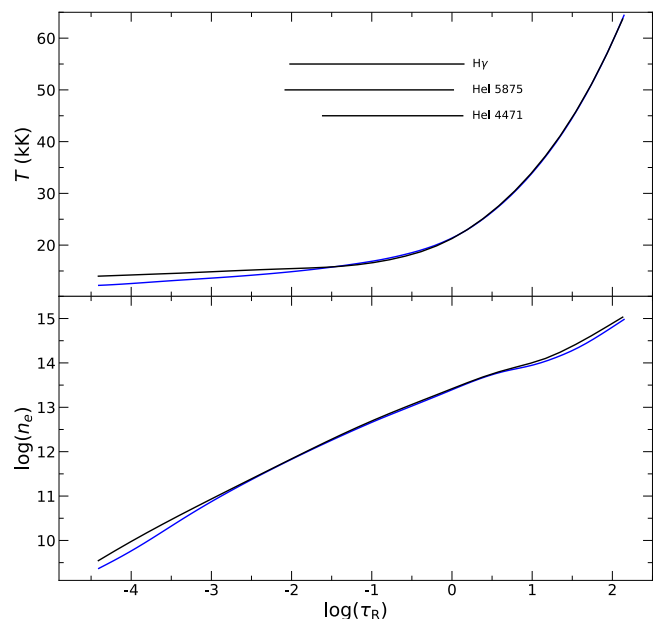


**Fig. 2.** Comparison of an ATLAS12 (blue) and TLUSTY (black lines) atmospheric structures for a model with  $T_{\text{eff}} = 20\,000\text{ K}$ ,  $\log g = 2.50$ , and  $\xi = 10\text{ km s}^{-1}$ . The upper and lower panel depict the run of temperature and the electron density, respectively, as a function of the Rosseland optical depth  $\tau_R$ . The line formation regions of H $\gamma$  and two lines of He I are indicated in the upper panel. See the text for a discussion.

bidden transitions. All collisional ionisation data were provided via the Seaton formula (Seaton 1962) using OP photoionisation threshold cross-sections or hydrogenic values.

Finally, synthetic spectra based on the non-LTE population numbers were calculated using an updated and extended version of SURFACE (Butler & Giddings 1985), employing refined fine-structure transition data and line-broadening theories. Oscillator strengths from Wiese et al. (1996) and Kurucz were replaced by data computed based on the multi-configuration Hartree-Fock method by Froese Fischer & Tachiev (2004) for O II (as for other elements and ions, also accounting for data from Froese Fischer et al. 2006), which was decisive in achieving the close match with observations. For both DETAIL and SURFACE an occupation probability formalism (Hummer & Mihalas 1988) – as realised by Hubeny et al. (1994) – was considered for hydrogen, in order to facilitate a better modelling of the series limits.

Grids of synthetic spectra were calculated with ATLAS12, DETAIL, and SURFACE – abbreviated as ADS in the following – for the entire parameter space of B-type supergiants. For the primary analysis of Balmer-lines and ionisation equilibria of all metals, effective temperatures  $T_{\text{eff}}$  were varied from 11 000 to 23 000 K in steps of 500 to 700 K, logarithmic surface gravities  $\log g$  from 1.70 to 3.70 (in cgs-units) in steps of 0.2 dex, and elemental abundances in steps of 0.2 dex, centred on cosmic abundance standard values (Nieva & Przybilla 2012; Przybilla et al. 2008a, 2013). For nitrogen, much higher values up to 1 dex above standard were covered because of the expected enrichment. Microturbulent velocities  $\xi$  were varied with increments of 4 km s<sup>-1</sup> initially and refined later to as low as 1 km s<sup>-1</sup>. The analysis was carried out – depending on the convergence of the model atmospheres – on grids ranging from 0 up to 16 km s<sup>-1</sup> in microturbulence, that is subsonic velocities.

We employed the Spectral Plotting and Analysis Suite (SPAS, Hirsch 2009) to compare the synthetic and observed spectra. The programme allows instrumental, (radial-tangential) macro-turbu-

<sup>3</sup> <http://kurucz.harvard.edu/atoms.html>

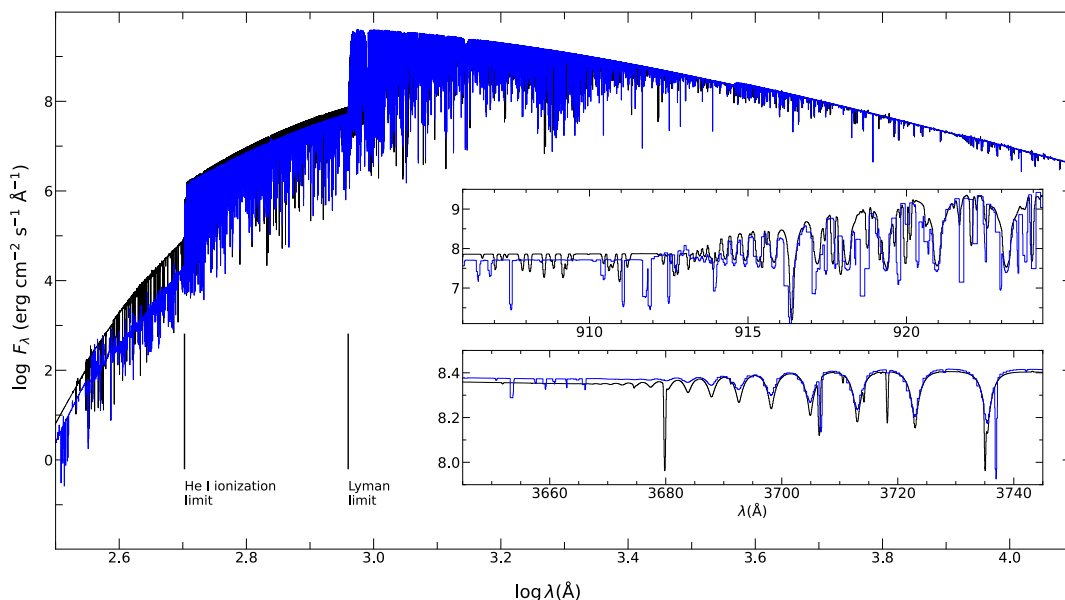


**Fig. 3.** Comparison of DETAIL (blue) and TLUSTY (black lines) SEDs for a model with  $T_{\text{eff}} = 20\,000\text{ K}$ ,  $\log g = 2.50$ , and  $\xi = 10\text{ km s}^{-1}$ . The locations of the Lyman- and He I ionisation limits are indicated towards the lower left. The insets focus on the Lyman and Balmer jumps, respectively.

lent and rotational broadening to be applied flexibly to the models and can be used to interpolate to the actual parameters with bi-cubic splines and fit up to three different parameters on the pre-calculated grid. To achieve this task, the programme employs the downhill simplex algorithm (Nelder & Mead 1965) to find minima in the  $\chi^2$ -landscape.

### 3.2. Comparison with full non-LTE models

Non-LTE effects gain in importance for more intense radiation fields (i.e. with increasing  $T_{\text{eff}}$ ) and reduced collision rates (i.e. with decreasing particle density). The atmospheric structures of B-type supergiants are therefore likely to be subject to non-LTE effects. Our hybrid non-LTE approach will only be successful if solutions from full non-LTE modelling can be closely recovered.

A comparison of a full non-LTE model atmosphere for solar metallicity (Grevesse & Sauval 1998) as adopted from the BSTAR grid (Lanz & Hubeny 2007) that was computed using the TLUSTY code (Hubeny & Lanz 1995) with an ATLAS12 structure is shown in Fig. 2, for model parameters  $T_{\text{eff}} = 20\,000\text{ K}$ ,  $\log g = 2.50$ , and  $\xi = 10\text{ km s}^{-1}$ . The temperature  $T$  and electron density  $n_e$  stratification as a function of Rosseland optical depth  $\tau_R$  is shown. Line-formation depths for some of the strongest diagnostic spectral features in the optical spectrum are also indicated, with the bulk of the metal lines being formed towards the inner boundary of this region. We want to note that the metallicity of the ATLAS12 model (computed explicitly for abundances according to Grevesse & Sauval 1998) was reduced by 0.2 dex in order to account empirically for non-LTE effects on the line blanketing. At the same metallicity, supergiant atmospheres in LTE and non-LTE show different temperature gradients because of the different amount of backwarming because of line blanketing and blocking. Empirically, a reduction of metallicity of LTE atmospheres by 0.2 dex can compensate this differences (see Fig. 2). The necessity for such an adjustment also follows on observational grounds. In order to reproduce the observed spectral lines, the real temperature gradient in the stellar atmosphere has to be matched by the model, as the different formation depths from line cores to the wings near the continuum-forming

layers of the entire ensemble of the lines map the temperature (and density) structure in the atmosphere in detail. Achieving a match between observation and model as shown in the figures in Appendix A requires the reproduction of the actual atmospheric structure by the model. To reproduce the observed SEDs, in particular for the cases where IUE spectrophotometry is available, also requires the reduction of the overall ATLAS atmosphere's metallicity. Otherwise the line absorption in the UV is stronger than observed. Thus, the empirical metallicity adjustment mimics non-LTE effects on the line opacity. The effect of a reduction of metallicity by 0.2 dex in the LTE model can be applied globally to supergiant models covering the range of effective temperatures investigated here, and only diminishes for models towards the main sequence. It can even be extended to early B-type supergiants as tested for a model with  $T_{\text{eff}} = 27\,000\text{ K}$ ,  $\log g = 3.00$ , and  $\xi = 10\text{ km s}^{-1}$ . In all cases the agreement of the adapted ATLAS12 stratifications with the TLUSTY structures is good throughout the photospheric line-formation depths, with differences less than 2% in  $T$  and 8% in  $n_e$  and only starts to deviate more for  $\log \tau_R < -2$ , where effects of the mass outflow would start to lead to departures from hydrostatic equilibrium in a real B-type supergiant atmosphere anyway.

The comparison of the TLUSTY and DETAIL non-LTE SEDs for the above parameters is shown in Fig. 3. The agreement longward of the Lyman limit is excellent overall, with the differences amounting to only a few percent. Also the hydrogen series limits (see the insets in Fig. 3) resemble each other closely because the same occupation probability formalism is employed in both codes. Larger differences occur at wavelengths below the Lyman limit, and in particular below the He I ionisation limit (locations indicated in Fig. 3), where TLUSTY predicts (significantly) higher ionising fluxes. The atmospheric layers that emit this extreme-ultraviolet radiation are located in the outermost regions of the model atmosphere. Consequently the differences are not relevant for the photospheric lines investigated here. Moreover, as these layers are not in hydrostatic equilibrium in real B-type supergiant atmospheres, the predictive power of both models presented here is limited and would be better investigated with hydrodynamical stellar atmosphere models.

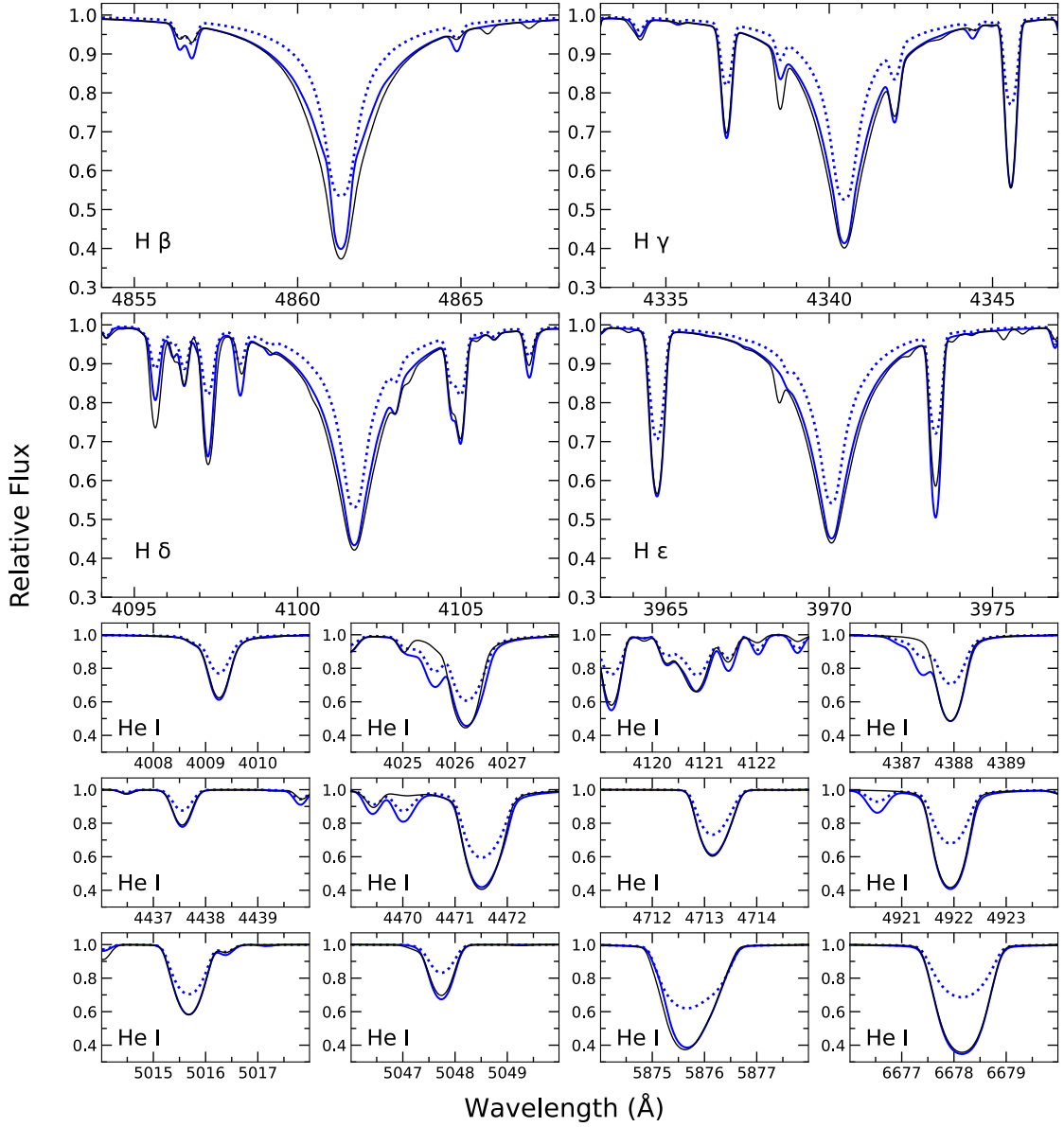


**Fig. 4.** Comparison of Balmer lines  $H\beta$ ,  $H\gamma$ ,  $H\delta$ ,  $H\epsilon$ , and selected lines of He I in synthetic spectra ( $T_{\text{eff}} = 20\,000\text{ K}$ ,  $\log g = 2.50$ , and  $\xi = 10\text{ km s}^{-1}$ ) calculated with Ads (blue lines) and TLUSTY/SYNPEC (black lines). The dotted blue lines correspond to a model computed with SURFACE only on an ATLAS12 atmospheric structure, i.e. representing an LTE solution using otherwise the same input data as in the Ads non-LTE model.

A further comparison of profiles for a selection of diagnostic hydrogen Balmer and He I lines as calculated by TLUSTY/SYNPEC and Ads for the above atmospheric parameters is shown in Fig. 4. The match between the two non-LTE synthetic spectra for these two chemical species is excellent except for some fine details. These concern the line cores of the Balmer lines, with the differences diminishing towards the higher series members, and some of the forbidden components of the He I lines, which are explained by the use of different broadening tables. However, the corresponding LTE model shows much weaker lines throughout, with the equivalent widths differing by factors of up to two to three. Overall, the differences increase towards the red. Pure LTE modelling is inapplicable for quantitative analyses of B-type supergiants.

In particular, the panels in Fig. 4 that show the Balmer lines cover a wider wavelength range and also depict spectral lines from other chemical species. While most of these cases show only moderate differences between the two non-LTE models,

some lines are noticeably discrepant. However, a straightforward comparison of these should not be made, because – in contrast to H and He, with their rather well-established atomic input data – most of the differences stem from the different atomic data used and the different assumptions made in the construction of the model atoms that were used in the two approaches. A detailed discussion of these aspects for the case of OB-type main-sequence stars was presented by Przybilla et al. (2011), which we do not repeat here. The basic conclusion is that the ability of different models to reproduce observations in a consistent way is decisive.

### 3.3. Turbulent pressure

The ATLAS12 code allows the effects of turbulent motions with velocity  $v_{\text{turb}}$  (i.e. the microturbulent velocity) on the model atmosphere computations to be taken into account. An additional turbulent pressure  $P_{\text{turb}}$  term is considered in the hydrostatic



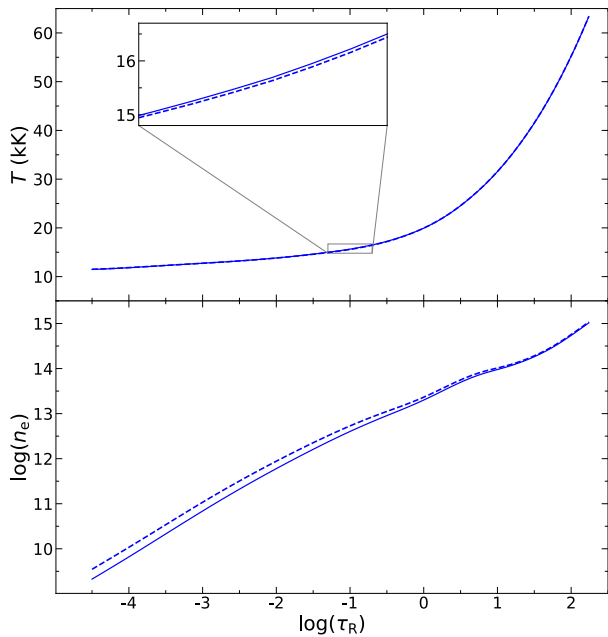


**Fig. 5.** Effects of turbulent pressure on the atmospheric stratification. Upper panel: temperature stratification, lower panel: electron density as a function of the logarithmic Rosseland optical depth. Displayed are ATLAS12 stratifications computed with (full line) and without considering turbulent pressure (dashed line) for  $T_{\text{eff}} = 18\,600$  K and  $\log g = 2.45$ , i.e. the atmospheric parameters for HD 14818.

equilibrium equation in the form of

$$P_{\text{turb}} = \frac{\rho v_{\text{turb}}^2}{2}, \quad (1)$$

where  $\rho$  is the atmospheric density. This additional term increases in importance for stars approaching the Eddington limit because of the diminishing rôle of the gas pressure, and for increasing  $v_{\text{turb}}$ . Since it is possible to enable and disable turbulent pressure in the model specification of ATLAS12, we can directly compare the effects of this term on the atmospheric structure and the synthetic spectra, while keeping all other parameters fixed. As a test, we chose the sample star HD 14818, at  $T_{\text{eff}} = 18\,600$  K,  $\log g = 2.45$ , and a derived high luminosity,  $\log L/L_{\odot} = 5.41$ . We expected to find a maximised impact on the model atmospheric structure because of its large  $\xi = 14$  km s<sup>-1</sup>.

Figure 5 visualises the run of temperature  $T$  (upper panel) and the logarithmic electron density  $n_e$  (lower panel) as a function of log-scale Rosseland optical depth  $\tau_R$  in the model atmosphere of HD 14818 for the two cases of turbulent pressure switched on and off, respectively. While the temperature hardly changes, with a maximum difference of about 50 K (being higher in the model with turbulent pressure), the electron density is noticeably lower for  $\log \tau_R < 0$  when turbulent pressure is considered because of the more extended atmosphere. Here, the absolute difference is about 0.12 dex in  $\log n_e$  at  $\log \tau_R = -1$ .

Figure 6 shows the effects of the models with and without turbulent pressure for otherwise identical parameters on various spectral line profiles. It can be seen that for the fitted lines of hydrogen (H $\delta$  and H $\epsilon$ ) the decreased density in the atmospheres with turbulent pressure corresponds to reduced pressure broadening of the Balmer line wings. Conversely, the model without turbulent pressure appears like a model with increased pressure broadening corresponding to the effect of an increase in surface gravity of about  $\Delta \log g \approx 0.05$  dex. A systematic effect can also

be detected in lines of helium and some metallic lines (Si II, C II, and S II) which mostly show enhanced line strength for models without turbulent pressure (the exception being the sulphur line at 4253 Å)<sup>4</sup>. The effect stems from a shift in the ionisation balance, yielding a higher degree of ionisation in the model that accounts for microturbulent pressure. This amounts to a reduction of equivalent widths of individual Si II lines by ~15 to 25% for the example of HD 14818 (the equivalent width of Si II  $\lambda 4130$  Å in Fig. 6 is e.g. reduced by 16%), while the lines of the main ionisation stage Si III remain essentially unchanged, and Si IV lines experience a slight strengthening by <5% in equivalent width. This impacts the atmospheric parameter and abundance determination to some small, but systematic, degree. Turbulent pressure is therefore considered in all analyses in the present work.

## 4. Spectral analysis

### 4.1. Atmospheric parameter and abundance determination

The basic atmospheric parameters were determined via an analysis of the spectral features of multiple ionisation stages of seven different chemical species (C, N, O, Ne, Al, Si, and Fe) as well as the analysis of the neutral helium lines and the Balmer lines of hydrogen. These parameters, effective temperature  $T_{\text{eff}}$ , surface gravity  $\log g$ , helium number fraction  $y$ , microturbulent velocity  $\xi$ , projected rotational velocity  $v \sin i$ , macroturbulence  $\zeta$  as well as the elemental abundances  $\varepsilon(X) = \log(X/H) + 12$ , were derived on the basis of spectrum synthesis, aiming at the reproduction of the detailed line profiles of features spanning the entire observed visual to near-infrared spectra. An iterative approach was employed to overcome ambiguities because of strong correlations, until all parameters were constrained in a consistent way and a single global solution for the synthetic spectrum was found that matches closely the entire observed spectrum.

#### 4.1.1. Effective temperature and surface gravity

In order to begin the analysis, an initial guess on the basis of spectral type and the shape and strength of the Balmer lines suffices for an estimation to within  $\Delta T_{\text{eff}} < 1500$  K and  $\Delta \log g < 0.4$  dex. Ambiguities in these two parameters arise due to their counteracting nature: in the regime of B-type supergiants, the Balmer lines grow weaker with  $T_{\text{eff}}$  as hydrogen is increasingly ionised, while increasing in strength with surface gravity due to the pressure broadening. Hence, multiple combinations of  $T_{\text{eff}}$  and  $\log g$  fit the observations. This means that Balmer line fitting alone is insufficient for a thorough analysis. The problem is solved by independently constraining  $T_{\text{eff}}$  and  $\log g$  using multiple ionisation equilibria of the studied elements, that is requiring that lines from the different ionisation stages of a chemical element are reproduced at the same elemental abundance value (within the mutual uncertainties). Table 4 summarises which ionisation balances were employed for the analysis of the sample stars, sorted from highest to lowest  $T_{\text{eff}}$ . Dots indicate that lines from the respective ionisation stage were analysed, the blue boxes then frame the achieved ionisation balance. Some combinations were useful throughout the entire  $T_{\text{eff}}$ -range, for example O I/II or Si II/III, while other ionisation stages appear

<sup>4</sup> We note that the panels depicting H $\delta$ , Si II  $\lambda 4130$  and He I  $\lambda 4120$  show lines of (and blends with) O II that systematically suggest a lower oxygen abundance. Originating from two multiplets sharing the same lower energy term, these lines appear too strong throughout the sample stars and were therefore excluded from the further quantitative analysis.



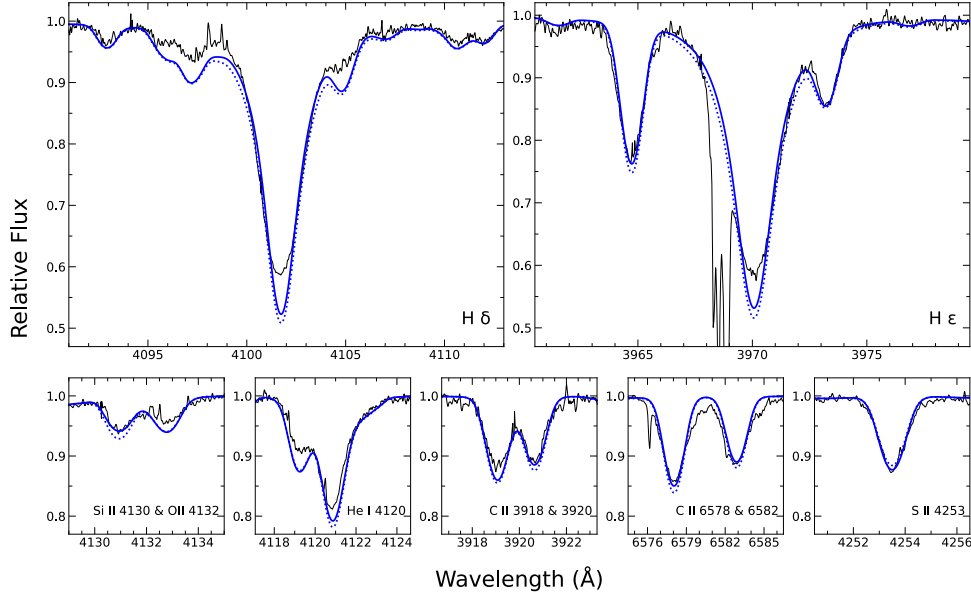


**Fig. 6.** Effects of turbulent pressure on line profiles. The solid blue line depicts the best fitting synthetic spectrum for several diagnostic lines in the observed spectrum of HD 14818 (black) derived from model atmospheres that account for turbulent pressure. The dotted blue line depicts the same solution without assuming turbulent pressure. The strong line in the blue wing of H  $\epsilon$  that is absent in the model is the interstellar Ca H line.

**Table 4.** Ionisation balances used for the atmospheric parameter determination.

ID #	$T_{\text{eff}}$ kK	C II/III	N I/II	O I/II	Ne I/II	Al II/III	Si II/III/IV	Fe II/III
11	19.7	●	● ●	● ●	● ●	●	● ● ●	●
13	19.5	● ●	● ●	● ●	●	● ●	● ● ●	● ●
2	18.6	●	●	● ●	● ●	●	● ● ●	●
10	17.2	●	●	● ●	●	●	● ● ●	● ●
9	15.6	●	● ●	● ●	●	● ●	● ● ●	● ●
14	14.7	●	● ●	● ●	●	● ●	● ●	● ●
4	14.6	●	● ●	● ●	●	● ●	● ● ●	● ●
1	14.1	●	● ●	● ●	●	● ●	● ●	● ●
7	14.0	●	● ●	● ●	●	● ●	● ●	● ●
12	13.7	●	● ●	● ●	●	● ●	● ●	● ●
3	13.6	●	● ●	● ●	●	● ●	● ●	● ●
5	12.8	●	● ●	● ●	●	● ●	● ●	● ●
8	12.7	●	● ●	● ●	●	● ●	● ●	● ●
6	11.9	●	● ●	● ●	●	● ●	● ●	● ●

only towards the highest  $T_{\text{eff}}$ -values, like C III, Ne II or Si IV and others such as N I, Al II or Fe II are no longer visible. Four to seven ionisation balances were matched simultaneously per star, with the tightest constraints occurring if three consecutive ionisation stages could be employed, as in the case of Si II/III/IV. Overall, ionisation balances are more sensitive to  $T_{\text{eff}}$ -variations, while the Balmer lines are more sensitive to  $\log g$ -variations. The finally adopted values of effective temperature and surface gravity, and their uncertainties, were then calculated as the arithmetic mean and standard deviation of the values implied by the individual indicators. In most of the sample objects, H $\alpha$  (see Fig. 1 for examples) had to be excluded from the analysis because of line asymmetries or the occurrence of emission due to the stellar wind. In the most luminous stars, H $\beta$ , H $\gamma$ , and even H $\delta$  may show signs of influence from the stellar wind and they were also omitted from the fitting process.

#### 4.1.2. Helium abundance

In the first step of the iterative procedure, the helium number density was set to the cosmic value of  $y = 0.089$  (Nieva & Przybilla 2012) in order to derive a satisfactory estimate for effective temperature and surface gravity. With these values, fitting of the weakest helium lines permitted a refined abundance estimate for helium with relative uncertainties between  $\delta y := \Delta y / y \approx 5\text{--}15\%$  to be derived. Stronger lines were generally excluded from the analysis, as they are less sensitive to abundance changes. Constraining the helium abundance is of importance not only per se. It strongly influences the molecular weight of the atmospheric elemental mixture and thereby changes the density and pressure stratification of the atmosphere, leading to changes in the derived surface gravity of up to  $\Delta \log g = 0.05$  dex. Further changes of the helium abundance in the following steps of the iteration scheme (i.e. after correcting  $T_{\text{eff}}$ ,  $\log g$ , and  $\xi$ ) were considered, but were found to lie within the uncertainties of the first determination.

#### 4.1.3. Microturbulence

Turbulent flows of matter on scales smaller than unit optical-depth can influence the shape and strength of spectral lines. They are parameterised as an ad-hoc microturbulence broadening parameter  $\xi$  (measured in  $\text{km s}^{-1}$ ) in addition to thermal broadening. Since this microturbulent velocity directly influences the broadening and therefore also the strength of the fitted metal lines, an incorrect value will lead to offsets in ionisation balances and consequently to inaccurate estimates of effective temperature. In fact, because of the pressure of the turbulent matter flows, microturbulence can also change the density structure of the atmosphere noticeably (see Sect. 3.3), affecting the surface gravity determination.

The appropriate value for  $\xi$  can be found by enforcing the criterion that the abundances derived from various spectral lines of a given element are independent of the strength of the spectral lines. For the analysis of our sample, we measured the equivalent widths  $W_\lambda$  of several trustworthy lines of N I/II and Si II/III/IV

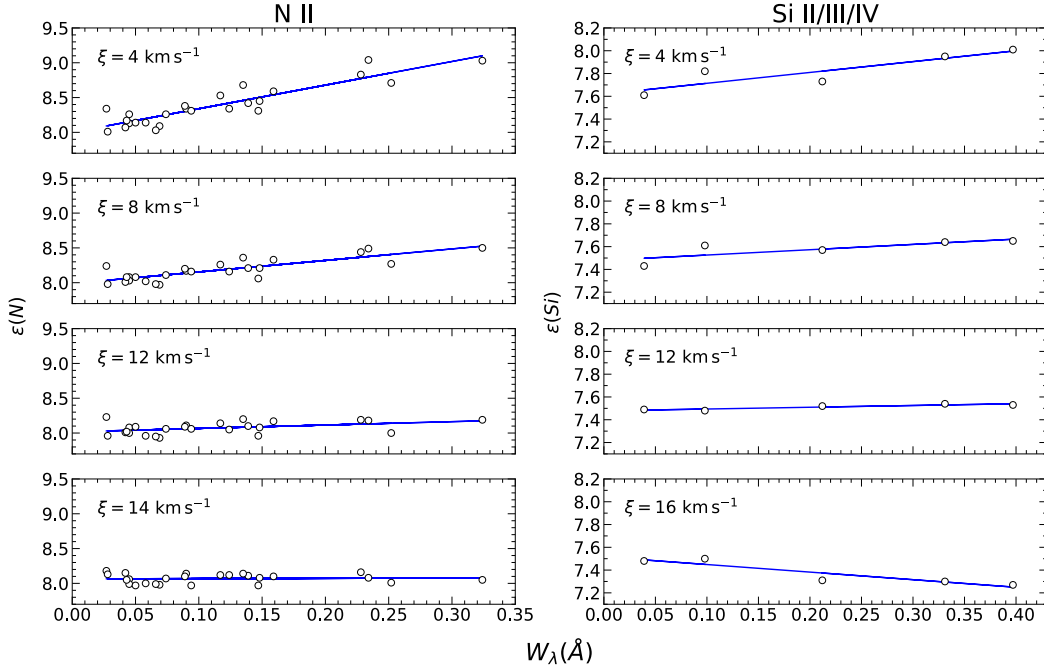


**Fig. 7.** Constraining the microturbulent velocity for HD 119646. The nitrogen (left panels) and silicon abundances (right panels) are displayed as a function of equivalent width for varying values of microturbulence, as indicated. The blue lines depict the best linear fit to the data.

as auxiliary quantities by direct integration of the observed spectral lines and compared their fitted abundances (from spectrum synthesis) for multiple values of  $\xi$ . This procedure is shown in Fig. 7: as  $\xi$  increases, the equivalent widths of the strong lines are affected more markedly by microturbulent broadening such that the abundance values necessary to fit them are reduced. The correct value for  $\xi$  is found when the fitted individual line abundances of a given element no longer correlate with their  $W_\lambda$  and the line-to-line abundance scatter is minimised. Uncertainties of the equivalent widths are of the order of the symbol size. In the given sample plot, the determinations are consistent with a microturbulent velocity of  $\xi \approx 14 \text{ km s}^{-1}$ . The value so derived was then checked for consistency with multiple lines of C II and Mg II in later steps of the atmospheric parameter iteration, and with Fe II/III lines in a further inspection. Corrections of  $\Delta\xi \approx 1\text{--}2 \text{ km s}^{-1}$  to the initial value were implied with respect to the initial value in some cases, such that a final value was obtained, fully consistent with the available indicators from several chemical species and ions.

#### 4.1.4. Projected rotational velocity and macroturbulence

Since the parameters of projected rotational velocity  $v \sin i$  and macroturbulent velocity  $\zeta$  do not affect the model atmosphere structure nor influence the line formation, their derivation is not related to time-expensive grid calculations. By convolution of the synthetic spectrum with the corresponding rotational and macroturbulent broadening functions (realised here by a radial-tangential model, Gray 1975) and by fitting weak metal lines of the observed spectra, we can find well-fitting values to within about 10% uncertainty for both  $v \sin i$  and  $\zeta$ . As has been pointed out in previous studies, multiple values of a pair of these parameters can lead to a similarly satisfactory fit to individual lines (e.g. Ryans et al. 2002; Farnstein & Przybilla 2012; Simón-Díaz & Herrero 2014). However, this ambiguity of solutions may be

minimised using suited line blends, see for example Fig. 11 of Przybilla et al. (2006a) or Fig. 5 of Farnstein & Przybilla (2012).

The existence of non-rotational broadening in B-type supergiants is well established. Physically, surface motions due to a sub-surface convection zone and stellar pulsations, among others, are the phenomena that are subsumed by the macroturbulence parameter (Simón-Díaz et al. 2017).

#### 4.1.5. Elemental abundances

Having derived a consistent solution for all primary atmospheric parameters, abundances of all investigated elements and ions were once more determined in a last step in order to allow a consistent fit of a single synthetic spectrum to the observed spectrum to be made. The final abundances of the individual elements were then computed as the arithmetic mean of the entire sample of fitted lines and the respective uncertainty as the  $1\sigma$  standard deviation. For the specification of the abundance of an element  $X$ , the customary logarithmic scale normalised to 12 was chosen, such that  $\varepsilon(X) = \log(X/H) + 12$ .

A selected sub-sample of lines in one of the analysed spectra is shown in Fig. 8 compared to the best-fitting model. The simultaneous reproduction of the Balmer lines, the helium and metal lines of different ionisation stages regardless of individual strength demonstrates the consistency of the derived solution.

#### 4.2. Stellar mass and age

The derivation of the spectroscopically accessible atmospheric parameters (in conjunction with the photometric data) allowed the determination of stellar masses. Effective temperature and surface gravity alone suffice to derive the initial, or zero-age main-sequence stellar mass  $M_{\text{ZAMS}}$ . For this, we define the spectroscopic luminosity  $\mathcal{L}$  as

$$\mathcal{L}/\mathcal{L}_\odot = \frac{(T_{\text{eff}}/T_{\text{eff},\odot})^4}{(g/g_\odot)}, \quad (2)$$

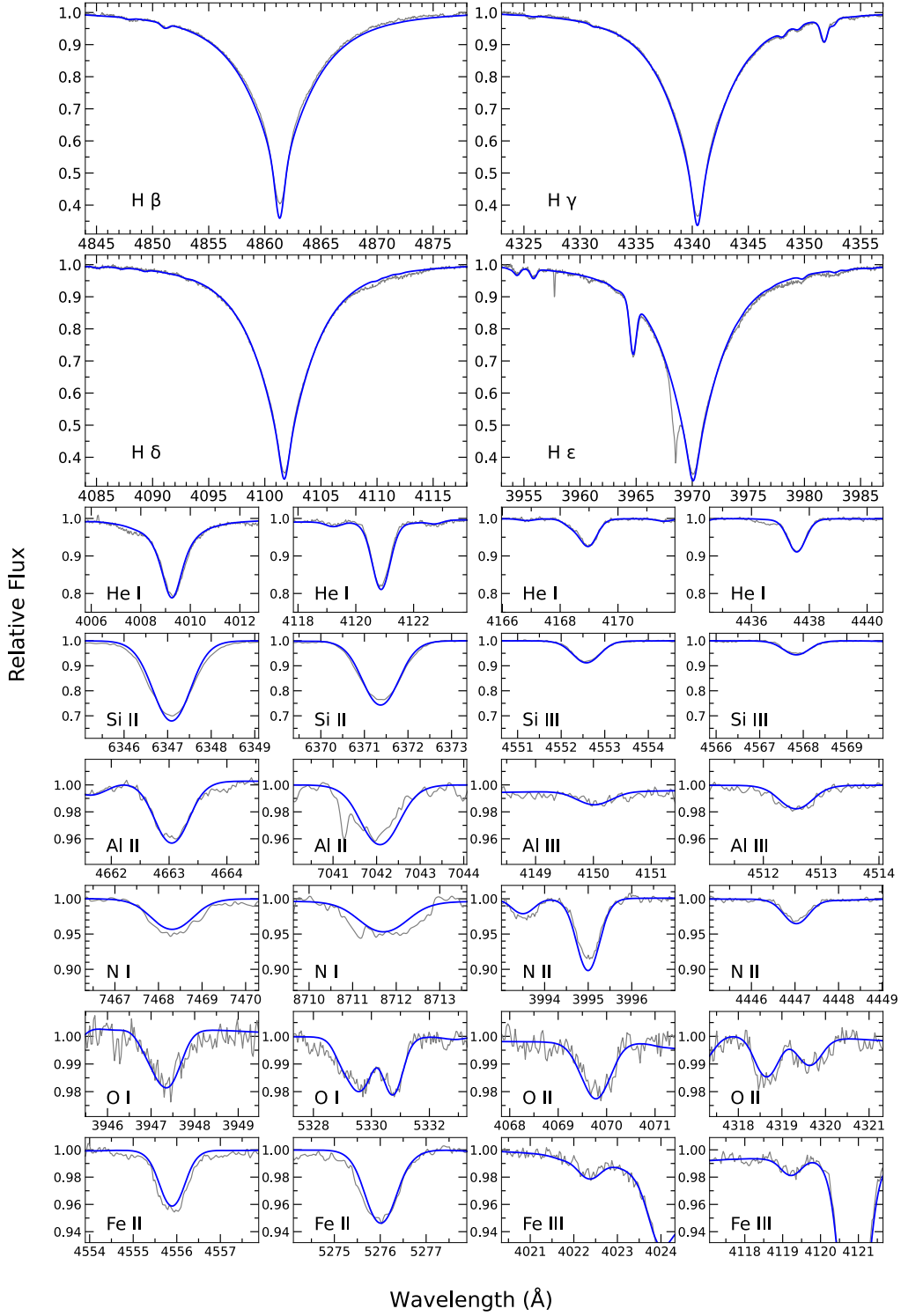


**Fig. 8.** Comparison of the observed spectrum for HD 125288 (black) with the model spectrum for some diagnostic lines at the best fitting parameters (blue lines). All lines of different atomic species and ionisation stages fit equally well, regardless of the strength of the individual lines.

(Langer & Kudritzki 2014), where the values for the solar effective temperature and surface gravity are  $T_{\text{eff},\odot} = 5777$  K and  $\log g_{\odot} = 4.44$ . Figure 9 shows the sample stars in a ‘spectroscopic’ Hertzsprung-Russell diagram (sHRD) with tracks of stellar evolution models according to Ekström et al. (2012) tracing the spectroscopic luminosity as a function of log-scale effective temperature. Interpolating on this grid of rotating models, we derived  $M_{\text{ZAMS}}$ . Under the assumption of a normal, single-star,

red-ward evolution in the HRD we then interpolated the model tracks in effective temperature to estimate the objects’ current masses  $M_{\text{evol}}$  in their respective evolved state. Depending on the initial mass of the objects, the evolved stars lost more than  $2 M_{\odot}$  through their stellar wind at the high mass limit of the sample and negligibly little ( $< 0.05 M_{\odot}$ ) for the least massive objects. From a comparison of rotating versus non-rotating models, it is apparent that the derived masses depend on the initial rotational

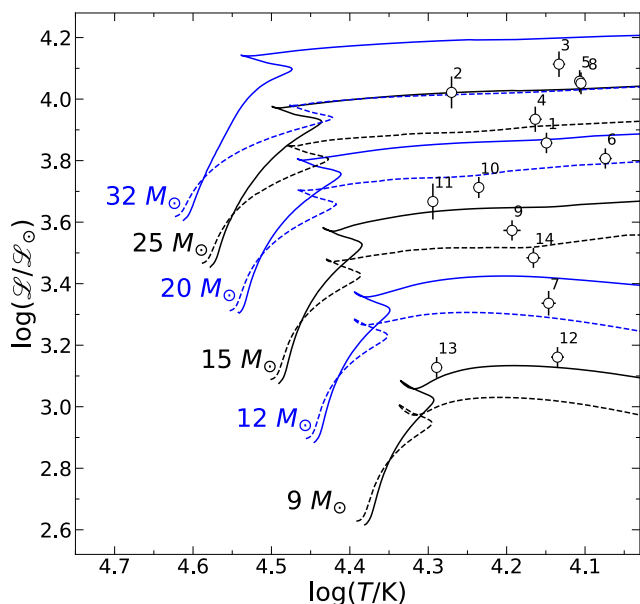


**Fig. 9.** Sample objects located in the spectroscopic HRD, spectroscopic luminosity versus log-scale effective temperature, with  $1\sigma$  error bars. Stellar evolution tracks (Ekström et al. 2012, for  $v_{\text{rot}} = 0.4v_{\text{crit}}$  and  $Z = 0.014$ ) ranging in ZAMS-masses from 9 to  $32 M_{\odot}$  are indicated in alternating colours of blue and black. The dashed lines depict the corresponding tracks for non-rotating models. Numbers denote the internal sample star IDs.

velocity. Specifically, we find that values of  $M_{\text{evol}}$  – as derived from non-rotating models – are larger by up to  $7 M_{\odot}$  at the high mass limit and about  $1 M_{\odot}$  larger at the lower mass limit of our sample. The initial rotational velocities of the sample stars on the ZAMS are unknown. However, mass loss (and therefore angular momentum loss) and the expansion to supergiant dimensions lead to a strong reduction of the rotational velocities, for example from about  $300 \text{ km s}^{-1}$  on the ZAMS to about  $50 \text{ km s}^{-1}$  for the rotating models of Ekström et al. (2012) at the boundary spanned by the stars ID#2 to #10 to #12 in Fig. 9. As our sample stars show  $v \sin i$ -values between about 20 to  $50 \text{ km s}^{-1}$  one would expect them to stem from stars with about average rotation on the ZAMS, and we can exclude initially very slow rotators with confidence, as they would be seen near zero  $v \sin i$  at the supergiant stage. We note, however, that the predictive power of the stellar evolution models needs to be treated with caution because of remaining uncertainties of the models. We therefore would like to stress that our results were obtained under the stated assumptions, and some small-scale systematic errors are likely to be present in the fundamental stellar parameters, but these cannot be quantified at the current time.

Ages of the stars were derived from interpolation in the isochrones for the (rotating) stellar evolution models of Ekström et al. (2012). Again, a normal red-ward evolution as single stars was assumed for the sample objects.

### 4.3. SED fitting

To fit the multi-band photometry and UV-data, synthetic ATLAS9<sup>5</sup> model SEDs of all sample objects were reddened according to the mean extinction law of Fitzpatrick (1999). The

flux of the observed magnitudes was calibrated with zero-points and fluxes according to the SVO Filter Profile Service<sup>6</sup> (Rodrigo et al. 2012; Rodrigo & Solano 2020). Models were then fitted for the two-parameter solution by Fitzpatrick (1999) – total-to-selective extinction  $R_V = A_V/E(B - V)$  and colour excess  $E(B - V)$  – in order to match the observations. The visual extinction  $A_V$  is then simply the product of the two parameters. A different approach had to be employed for HD 183143 because of a highly anomalous reddening law, see Ebenbichler et al. (2022) for details.

This method of examining the SED of our final solution generally worked very well and produced a high-precision characterisation of the interstellar medium along the sight lines towards the sample objects. In addition to being consistent with small uncertainties (see Sect. 5.6) the method can detect unusual features in the extinction curve, such as excess radiation in the WISE pass bands, hinting at black body radiation contributions to the stellar SED. Specifically, this process can detect anomalies in the composition of the interstellar medium along these sight lines, as in the case of HD 183143 mentioned above.

### 4.4. Spectroscopic distance

Having derived spectroscopic and fundamental parameters, as well as a precise reddening law for all sample objects, spectroscopic distances  $d_{\text{spec}}$  were calculated using an expression by Ramspeck et al. (2001)

$$d_{\text{spec}} = 7.11 \times 10^4 \sqrt{H_V M_{\text{evol}} 10^{0.4m_{V_0} - \log g}}, \quad (3)$$

where  $H_V$  denotes the Eddington flux, given in units of  $\text{erg cm}^{-2} \text{ s}^{-1} \text{ Hz}^{-1}$  at 550 nm,  $M_{\text{evol}}$  the evolutionary mass in units of  $M_{\odot}$ ,  $m_{V_0} = m_V - A_V$  the dereddened Johnson V magnitude in mag, and  $\log g$  the logarithmic surface gravity in cgs units. Equation 3 utilises the Vega flux calibration according to Heber et al. (1984) and provides distances in units of pc.

We have to stress once more that our  $M_{\text{evol}}$ -values were derived under the assumption of the overall applicability of the evolution tracks for rotating stars by Ekström et al. (2012). As we have argued in Sect. 4.2, the true initial rotational velocities of the sample stars are unknown, therefore some additional systematic uncertainty applies to the spectroscopic distances according to Eqn. 3 that may either increase or decrease the derived value.

These spectroscopic distances  $d_{\text{spec}}$  may be compared to distances  $d_{\text{Gaia}}$  derived from Gaia early data release 3 (EDR3) parallaxes (Gaia Collaboration et al. 2016, 2021). One potential issue is a mismatch of the Gaia distance with the spectroscopic distance because of a biased evolutionary mass, however the effects are only of order  $\propto M_{\text{evol}}^{1/2}$ . Alternatively, this can uncover potentially undetected models with the spectroscopic analysis. For instance, widely diverging estimations of distances can hint at an incorrect value for the surface gravity as this parameter contributes most of the uncertainty to the equation. It can, however, also uncover an unusual evolutionary development of an object in question (see Sect. 5.5). Gaia EDR3 parallaxes may also be affected by bias, such as increased uncertainties for the five brightest supergiants of the sample with Gaia G magnitude smaller than 6, or for objects with a large renormalised unit weight error (RUWE), like HD 51309 (ID#9), HD 125288 (ID#12), and HD 164353 (ID#14), which have a RUWE of about 2 – all other objects have RUWE-values around 1.

they can readily be employed for the comparison without requiring adjustment to the low-resolution observations.

<sup>6</sup> <http://svo2.cab.inta-csic.es/theory/fps/>

<sup>5</sup> The ATLAS9 starting models are equivalent to ATLAS12 models for the purpose of SED fitting, as the temperature structures are practically identical for nearly scaled-solar abundances (as realised here). However,



#### 4.5. Bolometric correction, luminosity and radius

For the calculation of the bolometric correction  $B.C.$ , we defined the bolometric magnitude  $m_{\text{bol}}$  for each star as the direct integration of its ATLAS9 model SED over all wavelengths, with the integration constant chosen such that a solar ATLAS9 model satisfies  $M_{\text{bol},\odot} = 4.74$  (see Bessell et al. 1998). The  $B.C.$  was then calculated as the difference between  $m_{\text{bol}}$  and the synthetic  $m_V$ .

In order to determine the stellar luminosity  $L$ , the absolute  $V$ -band magnitude  $M_V$  was calculated from the observed apparent magnitude  $m_V$  (Mermilliod 1997) utilising the derived spectroscopic distances  $d_{\text{spec}}$  (Sect. 4.4), as well as the total-to-selective extinction  $R_V$ , and colour excess  $E(B - V)$  (Sect. 4.3) in the distance modulus. Correction of  $M_V$  by  $B.C.$  yielded the absolute bolometric magnitude  $M_{\text{bol}}$ , from which  $L$  was derived using the above value for  $M_{\text{bol},\odot}$ . The effective temperature and luminosity were finally utilised to determine the stellar radius  $R$  by application of the Stefan-Boltzmann law.

## 5. Results

The results of the analysis of the sample stars are summarised in Table 5. The parameters listed are: internal identification number, HD-designation, effective temperature, surface gravity, surface helium abundance, microturbulent, projected rotational and macroturbulent velocities, total-to-selective extinction parameter, colour excess, bolometric correction, evolutionary mass, radius, luminosity, evolutionary age, spectroscopic and Gaia EDR3 distances (probabilistic estimations of 'photogeometric' distances, Bailer-Jones et al. 2021). The respective uncertainties, given in the line below the observed values, denote  $1\sigma$ -intervals.

### 5.1. Atmospheric and fundamental stellar parameters

For the effective temperature and surface gravity, the uncertainties roughly match the values derived in previous work analysing BA-type supergiants with a similar analysis approach as employed here (Firnstein & Przybilla 2012), with  $\delta T_{\text{eff}} \approx 1\text{--}3\%$  and  $\Delta \log g \approx 0.05$  dex. Abundances of helium were fitted with uncertainties of  $\delta y \approx 5\text{--}15\%$  owing to the line-to-line scatter from the weakest He I features analysed, that is those most sensitive to abundance variations.

The uncertainty of the microturbulent velocity is generally limited by the size of the grid used during the fitting process. Though observed values of  $\xi$  were in some cases inspected on scales of  $1 \text{ km s}^{-1}$ , a conservative estimate of  $\Delta \xi \approx 2 \text{ km s}^{-1}$  is adopted throughout. Projected rotational velocities show relative uncertainties amounting to typically  $\delta v \sin(i) \approx 10\text{--}15\%$  owing to the degeneracy in the joint derivation with macroturbulent velocities. For the macroturbulence  $\zeta$  the uncertainties were estimated at a value of  $5 \text{ km s}^{-1}$ .

A similar but weaker ambiguity in deduced values is generally present in the estimation of total-to-selective extinction parameter and colour excess. The fitting procedure described in Sect. 4.3 produces error margins of the order of  $\Delta R_V \approx 0.1$  and  $\Delta E(B - V) \approx 0.03$  mag. Although the exact margins in this derivation depend on the available data (in particular in the UV-range) these values generally represent the typical uncertainties for the entire sample. For the derivation of the  $B.C.$  no detailed analysis of uncertainties was conducted, though variation of parameters in input models hinted at an uncertainty range of  $\Delta B.C. \approx 0.04\text{--}0.06$  mag for both hotter and cooler sample stars.

The parameter of evolved mass  $M_{\text{evol}}$  was derived using the ZAMS mass estimates, tracing their mass loss in evolution tracks by Ekström et al. (2012), see Sect. 5.7, such that the uncertainties of the evolved masses are assumed to be identical to the ZAMS mass uncertainty of about  $\delta M_{\text{ZAMS}} = \delta M_{\text{evol}} \approx 5\%$ . Radii of sample objects show relative errors of about  $\delta R \approx 10\%$ , stemming largely from the associated uncertainty in luminosity, which amounts to typically  $\Delta \log L/L_{\odot} \approx 0.1$  dex. The distances derived in this work show consistent relative uncertainties of  $\delta d_{\text{spec}} \approx 10\%$ , matching the sample mean relative difference between the deduced values and those derived from parallactic distances by the Gaia mission (see Sect. 5.5). The fundamental parameters can be expected to be subject to a small amount of additional systematic error because a set of stellar evolution models for a particular rotational velocity were adopted, see the discussion in Sect. 4.2.

### 5.2. Comparison with previous analyses

Many of our sample stars were analysed in previous studies that employed full non-LTE model atmospheres. For comparison, data from the following studies were considered:

- i) Markova & Puls (2008) employed FASTWIND for their analyses. They utilised hydrogen, helium, and Si II/III/IV lines to derive temperature, surface gravity, and microturbulence iteratively. The derivation of projected rotational velocities was based on the analysis of the shape of the Fourier transform (FT) of absorption lines (Gray 1975; Simón-Díaz & Herrero 2007). Two objects are in common.
- ii) Searle et al. (2008) used the stellar atmosphere codes TLUSTY and CMFGEN (Hillier & Miller 1998). To estimate the temperature, the diagnostic silicon lines of Si IV 4089 and Si III 4552–4574 Å were used in supergiants of spectral types B0 to B2 and Si II 4128–4130 and Si III 4552–4574 Å for B2.5 to B5 supergiants. The luminosity was then constrained by inferred values of the absolute visual magnitude  $M_V$  and corrected if necessary. Surface gravity  $\log g$  was determined by fitting H $\gamma$  and H $\delta$ . The microturbulent velocity was determined by analysing the Si III triplet lines. Three objects are in common.
- iii) Fraser et al. (2010) used the hydrostatic line-blanketed non-LTE codes TLUSTY and SYNSPEC (Hubeny 1988; Hubeny & Lanz 1995) that consider plane-parallel geometry. Effective temperatures were estimated on the basis of silicon ionisation equilibria and surface gravities from a fit of the H $\gamma$  and H $\delta$  lines. For the determination of microturbulence they relied solely on the analysis of the Si III triplet at 4552–4574 Å and projected rotational velocities were derived using the FT method. Six objects are shared.
- iv) Simón-Díaz et al. (2017) used the hydrodynamic line-blanketed non-LTE code FASTWIND (Santolaya-Rey et al. 1997; Puls et al. 2005) that accounts for spherical geometry, following the spectroscopic analysis strategy described by Castro et al. (2012). They analysed H $\beta$ , H $\gamma$ , H $\delta$ , multiple lines of He I, as well as the silicon multiplets Si II 4128–4130 Å, Si III 4552–4574 Å, and Si IV 4116 Å to derive  $T_{\text{eff}}$  and  $\log g$ . For the derivation of projected rotational velocities they used the IACOB-BROAD tool (Simón-Díaz & Herrero 2014) on lines of O, Si, Mg, and C, depending on the spectral type of the star. Eight objects are common to the present work.

Furthermore, a sample of 25 O9.5–B3 Galactic supergiants were analysed by Crowther et al. (2006) based on CMFGEN models. We do not compare with this paper since it has only one object (HD 14818) in common with the present work.

**Table 5.** Stellar parameters of the sample objects.

ID#	Object	$T_{\text{eff}}$ kK	$\log g$ (cgs)	$y$	$\xi$ km s <sup>-1</sup>	$v \sin i$ km s <sup>-1</sup>	$\zeta$	$R_V$	$E(B - V)$ mag	$B.C.$ mag	$M_{\text{evol}}$ $M_{\odot}$	$R$ $R_{\odot}$	$\log L/L_{\odot}$	$\log \tau_{\text{evol}}$ yr	$d_{\text{spec}}$ pc	$d_{\text{Gaia}}^a$ pc
1	HD 7902	14.1	2.13	0.089	9	36	35	3.16	0.58	-0.999	19.2	64	5.16	6.98	2900	2487
		$\pm 0.2$	0.05	0.006	2	5	5	0.1	0.03		0.8	7	0.09	0.3	280	<sup>110</sup> <sub>80</sub>
2	HD 14818	18.6	2.45	0.095	14	48	40	3.09	0.56	-1.645	23.6	49	5.41	6.89	2150	2121
		$\pm 0.3$	0.07	0.008	2	6	5	0.1	0.03		1.9	6	0.11	0.03	250	<sup>150</sup> <sub>110</sub>
3	HD 25914	13.6	1.81	0.092	11	35	40	2.97	0.76	-0.943	25.7	106	5.54	6.86	6030	5431
		$\pm 0.2$	0.06	0.004	2	5	5	0.1	0.03		1.6	13	0.10	0.03	640	<sup>790</sup> <sub>440</sub>
4	HD 36371	14.6	2.11	0.086	11	36	35	3.35	0.52	-1.081	21.1	68	5.28	6.94	1200	1214
		$\pm 0.3$	0.06	0.005	2	5	5	0.1	0.03		1.2	8	0.10	0.03	130	<sup>380</sup> <sub>220</sub>
5	HD 183143	12.8	1.76	0.099	7	37	27	3.3	1.22	-0.793	24.2	109	5.46	6.88	1530	2168
		$\pm 0.2$	0.05	0.005	2	5	5	0.1	0.03		1.4	15	0.11	0.03	170	<sup>120</sup> <sub>120</sub>
6	HD 184943	11.9	1.88	0.099	9	35	25	2.97	0.84	-0.600	17.7	82	5.07	7.02	4040	4090
		$\pm 0.2$	0.05	0.002	2	6	5	0.1	0.03		0.8	10	0.10	0.04	400	<sup>240</sup> <sub>240</sub>
7	HD 191243	14.0	2.64	0.087	8	27	25	2.88	0.33	-0.972	11.0	27	4.39	7.32	1220	1205
		$\pm 0.3$	0.06	0.011	2	6	5	0.1	0.03		0.5	3	0.09	0.05	120	<sup>30</sup> <sub>30</sub>
8	HD 199478	12.7	1.76	0.107	8	40	40	3.03	0.62	-0.783	24.0	111	5.46	6.88	2440	2423
		$\pm 0.2$	0.05	0.004	2	6	5	0.1	0.03		1.3	12	0.09	0.03	230	<sup>230</sup> <sub>220</sub>
9	HD 51309	15.6	2.59	0.081	10	30	35	3.08	0.11	-1.236	13.7	32	4.72	7.17	950	1108
		$\pm 0.4$	0.05	0.003	2	6	5	0.1	0.03		0.5	4	0.09	0.04	90	<sup>410</sup> <sub>210</sub>
10	HD 111990	17.2	2.62	0.089	12	40	40	3.3	0.45	-1.464	16.1	33	4.94	7.07	1940	2418
		$\pm 0.3$	0.05	0.003	2	6	5	0.1	0.03		0.7	4	0.09	0.04	180	<sup>160</sup> <sub>180</sub>
11	HD 119646	19.7	2.9	0.100	14	37	40	3.53	0.34	-1.781	15.4	23	4.87	7.10	1620	1721
		$\pm 0.2$	0.07	0.009	2	6	5	0.1	0.03		1.2	3	0.11	0.05	190	<sup>80</sup> <sub>70</sub>
12	HD 125288	13.7	2.77	0.094	6	23	30	3.65	0.30	-0.934	9.3	21	4.14	7.46	390	438
		$\pm 0.3$	0.05	0.007	2	4	5	0.1	0.03		0.3	2	0.09	0.05	40	<sup>50</sup> <sub>30</sub>
13	HD 159110	19.5	3.42	0.095	3	17	15	3.3	0.22	-1.826	9.3	10	4.11	7.45	1290	1362
		$\pm 0.3$	0.05	0.001	2	4	5	0.1	0.03		0.3	1	0.09	0.05	120	<sup>80</sup> <sub>70</sub>
14	HD 164353	14.7	2.57	0.091	8	20	32	3.61	0.19	-1.081	12.6	31	4.60	7.22	620	797
		$\pm 0.3$	0.05	0.004	2	4	5	0.1	0.03		0.4	4	0.09	0.04	60	<sup>200</sup> <sub>130</sub>

**Notes.** Uncertainties are  $1\sigma$ -values, except where noted otherwise. <sup>(a)</sup> Gaia Collaboration et al. (2016, 2021) - distances and uncertainties correspond to 'photogeometric distances' and associated 14<sup>th</sup> and 86<sup>th</sup> confidence percentiles (Bailer-Jones et al. 2021).

Figure 10, panel a, shows a comparison of the effective temperatures from the literature  $T_{\text{eff}}^{\text{lit}}$  with those derived here. An overall good correlation is found with a mean relative difference  $\delta T_{\text{eff}}^{\text{comp}} = \frac{1}{N-1} \sum_i (T_{\text{eff},i} - T_{\text{eff},i}^{\text{lit}}) / T_{\text{eff},i}^{\text{lit}}$  of less than 1%, and a standard deviation of 5%. Two objects, HD 119646 and HD 183143 (marked with open symbols), differ by  $\sim 12\%$  in literature versus present-work  $T_{\text{eff}}$  with both higher and lower values realised. Some objects are present in two or more of the cited studies, in which case the objects are depicted as diamonds. For such objects the values never scatter by more than about 1000 K.

The comparison of surface gravities is shown graphically in Fig. 10, panel b. Again, values occurring in more than one study are depicted as diamonds, but in this comparison, some objects show a larger scatter among the various studies. For HD 164353 estimates range from  $\log g = 2.46$  in Simón-Díaz et al. (2017),  $\log g = 2.50$  in Fraser et al. (2010) to  $\log g = 2.75$  in Searle et al. (2008); for HD 191243 Simón-Díaz et al. (2017) derive  $\log g = 2.45$ , while Markova & Puls (2008) finds  $\log g = 2.61$  and Searle et al. (2008) again give the largest value of  $\log g = 2.75$ , that is differences up to a factor of 2. Treating the literature values as one complete comparison set, a systematic offset towards higher  $\log g$  values in the present work may be noticed. One may speculate that this trend may be due to the inclusion of  $P_{\text{turb}}$  in our analysis, resulting in a systematic increase of  $\log g$ . However, we have demonstrated that the effect of this term in the model is limited to  $\sim 0.05$  dex even in objects with large microturbulent velocities close to the Eddington limit (see Sect. 3.3). In light of the large uncertainties of the literature values, small number statistics, and general differences between the trends in the dif-

ferent comparison studies, we cannot draw definite conclusions on the origin of these differences.

Figure 10, panel c shows the comparison of microturbulent velocities. Both the correlation of literature and present values, as well as the agreement between literature values of different studies is poor. In the case of HD 191243, a maximum difference of  $\Delta\xi = 13 \text{ km s}^{-1}$  is found between Markova & Puls (2008) and our work on the one hand and Searle et al. (2008) on the other. Overall, our assessments of microturbulent velocity are systematically lower by  $\sim 10 \text{ km s}^{-1}$  than the literature values, with the exception of Markova & Puls (2008). While our microturbulent velocities remain subsonic, literature values are often found to be supersonic. Such systematically lower microturbulent velocities were also found in previous work on B-type main-sequence stars (Nieva & Przybilla 2012), where a broad variety of microturbulence indicators were employed versus the usual reliance on the Si III 4552–4574 Å triplet alone. We note that microturbulence velocities were not provided by Simón-Díaz et al. (2017).

Finally, a comparison of projected rotational velocities is shown in Figure 10, panel d. Good agreement is achieved overall, though there are some small-scale differences between the compared works. Values by Simón-Díaz et al. (2017) agree very well with ours, showing little to no offset and small scatter, while values derived in this work are systematically larger by  $\sim 4 \text{ km s}^{-1}$  in comparison with data of Fraser et al. (2010). The only significant outlier is the  $v \sin i$ -value of HD 191243 in the work by Markova & Puls (2008), which is likely a statistical outlier, given the good accordance of the corresponding value in Simón-Díaz et al. (2017).

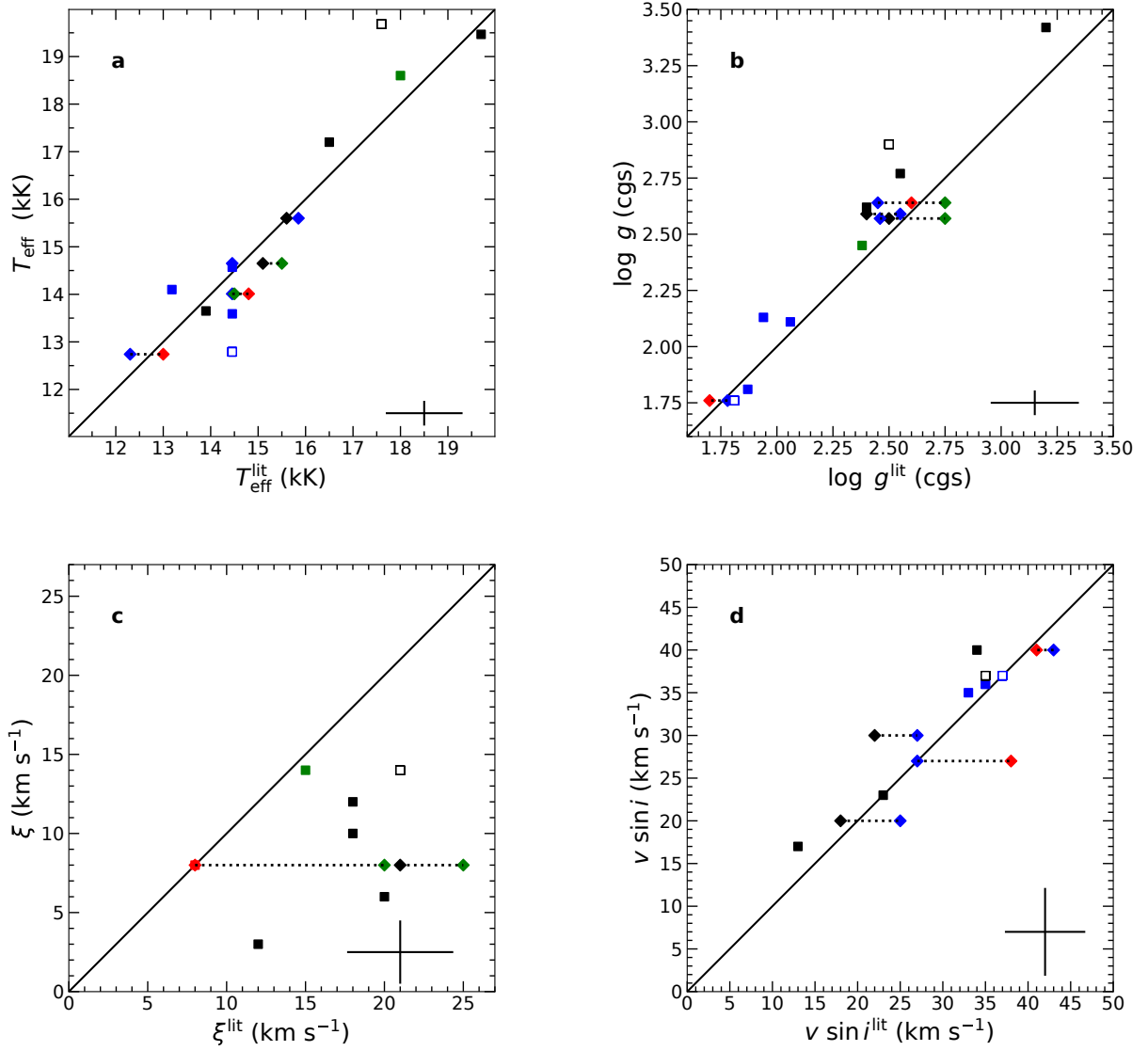


**Fig. 10.** Comparison of values for effective temperature  $T_{\text{eff}}$  (panel a), surface gravity  $\log g$  (panel b), microturbulence  $\xi$  (panel c), and projected rotational velocity  $v \sin i$  (panel d) as derived in the present work with previous studies: Fraser et al. (2010, black symbols), Simón-Díaz et al. (2017, blue), Markova & Puls (2008, red), and Searle et al. (2008, green). In cases in which an object is present in two or multiple studies the values are depicted by diamonds and connected with dotted lines. The symbols for HD 183143 and HD 119646 are marked by open symbols. For better visibility, the mean uncertainties are indicated in the lower right corner.

### 5.3. Elemental abundances and stellar metallicity

The mean abundances of all the metal species studied here (which constitute the ten most abundant elements besides hydrogen and helium) along with their uncertainties and the number of analysed lines are summarised in Table 6. In addition, the resulting metallicities of the sample stars are shown. For a conservative estimate of the error margins the  $1\sigma$  sample standard deviation of individual line abundances was chosen, as tests on single line statistical uncertainty resulted in unreasonably low margins. In general, these statistical uncertainties range from  $\sim 0.05$ – $0.10$  dex, and rarely exceed the latter value. The number of lines analysed per species and object is at least two in very few cases and usually much larger. Standard errors of the mean therefore amount to typically  $0.02$ – $0.03$  dex for the elemental abundances in each star. Metal mass fractions  $Z$  (‘metallicities’) of the sample stars were calculated from the available metal abundances and are indicated in the last column of Table 6. As these cover

the ten most abundant metal species these should be representative for the sum of all metals.

The systematic uncertainties depend primarily on the quality of the respective model atoms and on the uncertainties in effective temperatures, surface gravities, and microturbulent velocities, see for example the discussions by Przybilla et al. (2000, 2001a,b) and Przybilla & Butler (2001). Given the experience gained in these works, we expect the systematic uncertainties of the elemental abundances to amount to  $\sim 0.1$  dex.

The derivation of abundances for all chemical species that show spectral lines in the optical allowed global synthetic spectra to be calculated, that is one model spectrum based on the derived atmospheric parameters and abundances per star. This also includes the blended features that were excluded from the chemical analysis. As can be expected from the small abundance uncertainties, the reproduction of the observed spectra by the global synthetic spectrum is excellent overall, as shown for the exemplary case of HD 164353 in Appendix A, Figs. A.1 to A.8.

**Table 6.** Metal abundances  $\varepsilon(X) = \log(X/H) + 12$  and metallicity  $Z$  (by mass) of the sample objects.

ID#	Object	C	N	O	Ne	Mg	Al	Si	S	Ar	Fe	Z
1	HD 7902	8.25 (9) ±0.04	8.27 (27) 0.06	8.75 (17) 0.05	7.96 (12) 0.05	7.51 (8) 0.07	6.44 (5) 0.09	7.54 (10) 0.09	6.96 (13) 0.07	6.41 (4) 0.07	7.59 (24) 0.11	0.014 0.002
2	HD 14818	8.00 (9) ±0.05	8.33 (24) 0.09	8.50 (22) 0.06	8.08 (6) 0.05	7.49 (4) 0.11	6.17 (5) 0.05	7.62 (8) 0.07	6.94 (5) 0.03	6.54 (4) 0.05	7.37 (17) 0.07	0.011 0.002
3	HD 25914	8.09 (8) ±0.09	8.22 (25) 0.09	8.58 (18) 0.05	7.96 (11) 0.06	7.28 (3) 0.11	6.19 (4) 0.06	7.29 (9) 0.08	6.72 (10) 0.09	6.38 (3) 0.06	7.50 (22) 0.07	0.010 0.002
4	HD 36371	8.10 (11) ±0.08	8.33 (27) 0.06	8.57 (26) 0.07	8.06 (14) 0.05	7.40 (5) 0.07	6.34 (3) 0.02	7.44 (10) 0.08	6.96 (14) 0.09	6.34 (7) 0.05	7.48 (26) 0.11	0.012 0.002
5	HD 183143	8.31 (9) ±0.07	8.69 (26) 0.06	8.78 (12) 0.05	8.09 (12) 0.07	7.69 (6) 0.09	6.44 (6) 0.06	7.58 (7) 0.06	7.10 (10) 0.08	6.56 (2) 0.08	7.66 (26) 0.10	0.018 0.002
6	HD 184943	8.43 (6) ±0.04	8.63 (19) 0.06	8.84 (8) 0.06	8.02 (12) 0.05	7.63 (4) 0.01	6.47 (7) 0.08	7.66 (7) 0.08	7.05 (12) 0.07	6.63 (2) 0.12	7.75 (16) 0.10	0.019 0.002
7	HD 191243	8.28 (9) ±0.08	8.24 (35) 0.08	8.72 (27) 0.08	7.94 (14) 0.05	7.57 (9) 0.05	6.34 (4) 0.13	7.52 (10) 0.06	6.98 (13) 0.07	6.39 (7) 0.07	7.62 (31) 0.09	0.014 0.002
8	HD 199478	8.20 (6) ±0.05	8.63 (26) 0.06	8.74 (15) 0.08	7.99 (12) 0.05	7.64 (5) 0.08	6.40 (4) 0.09	7.58 (7) 0.06	7.11 (13) 0.08	6.54 (5) 0.09	7.76 (23) 0.09	0.016 0.002
9	HD 51309	8.29 (12) ±0.06	8.23 (27) 0.05	8.71 (24) 0.07	8.02 (11) 0.05	7.52 (8) 0.09	6.52 (3) 0.10	7.56 (9) 0.06	7.03 (13) 0.08	6.41 (9) 0.09	7.55 (28) 0.16	0.014 0.002
10	HD 111990	8.13 (13) ±0.06	8.21 (31) 0.06	8.65 (17) 0.08	8.06 (12) 0.07	7.50 (3) 0.06	6.17 (6) 0.11	7.50 (7) 0.05	7.07 (11) 0.09	6.44 (10) 0.08	7.49 (22) 0.07	0.012 0.002
11	HD 119646	8.24 (15) ±0.08	8.02 (24) 0.06	8.65 (16) 0.05	8.15 (11) 0.04	7.51 (5) 0.06	6.22 (5) 0.08	7.54 (7) 0.03	7.01 (4) 0.09	6.47 (7) 0.05	7.41 (19) 0.06	0.012 0.002
12	HD 125288	8.35 (8) ±0.07	8.50 (29) 0.07	8.80 (20) 0.06	8.06 (12) 0.06	7.54 (10) 0.09	6.26 (6) 0.07	7.62 (11) 0.09	7.11 (13) 0.05	6.52 (10) 0.08	7.60 (34) 0.08	0.017 0.002
13	HD 159110	8.53 (19) ±0.06	7.92 (35) 0.05	8.85 (22) 0.07	8.10 (21) 0.07	7.49 (10) 0.06	6.34 (5) 0.04	7.54 (7) 0.10	7.20 (16) 0.09	6.54 (16) 0.06	7.55 (21) 0.08	0.016 0.002
14	HD 164353	8.31 (10) ±0.04	8.37 (33) 0.06	8.81 (20) 0.06	8.05 (19) 0.06	7.51 (7) 0.05	6.32 (4) 0.04	7.65 (10) 0.10	7.11 (12) 0.07	6.47 (12) 0.08	7.63 (32) 0.11	0.016 0.002
	CAS <sup>a,b</sup>	8.35 ±0.04	7.79 0.04	8.76 0.05	8.09 0.05	7.56 0.05	6.30 0.07	7.50 0.06	7.14 0.06	6.50 0.08	7.52 0.03	0.014 0.002

**Notes.** Uncertainties are  $1\sigma$ -values from the line-to-line scatter. Numbers in parentheses quantify the analysed lines.

<sup>(a)</sup> Nieva & Przybilla (2012) <sup>(b)</sup> Przybilla et al. (2013)

Apart from some occasional very weak features, for instance of S II where the model atom would need to be extended to include more energy levels, all important stellar spectral lines are included in the spectrum synthesis. Noticeable omissions are several interstellar ('IS') atomic features, such as the Ca H and K lines, the Na D lines, a K I resonance line<sup>7</sup>, the diffuse interstellar bands (DIBs), and the telluric absorption features typically due to O<sub>2</sub> and H<sub>2</sub>O bands that occur with increasing frequency towards the near-IR. Some residual problems remain for a few stellar lines, for example the mismatch of the H $\alpha$  Doppler core, which is likely caused by the (weak) stellar wind in this object and not accounted for by the present modelling approach. The widths of the two strongest He I lines  $\lambda$ 5875 and 6678 Å are not perfectly matched. It would certainly be worthwhile to investigate this further as the widths of all other helium lines are reproduced well, but this is beyond the scope of the present paper. A few metal lines also show somewhat larger deviations, such as the C II  $\lambda$ 6578/82 Å doublet, which may hint at the possibility that the model atom may need to be improved with respect to these lines. However, in view of the overall solution these are minor details, the few discrepant features were not considered for the analysis.

Previous work on abundances of early B-type stars in the solar neighbourhood (distances out to ~400 pc from the Sun) has

<sup>7</sup> Only the K I  $\lambda$ 7698.9 Å line is clearly visible in this case, while the other fine-structure component K I  $\lambda$ 7664.9 Å overlaps with a saturated telluric O<sub>2</sub> line (see e.g. Kimeswenger et al. 2021), which depends on the radial velocity of the target star.

found chemical homogeneity, establishing a present-day cosmic abundance standard (CAS, Nieva & Przybilla 2012; Przybilla et al. 2013), see Table 6. Such a comparison of abundances between the present sample stars and the CAS is inappropriate here because of the widely different distances of the sample objects from the Galactic centre (see Sect. 5.5), for example ~7 kpc for HD 184943 versus ~13 kpc for HD 25914. For the same reason, an important test to verify the independence of abundances of atmospheric parameters such as  $T_{\text{eff}}$  and  $\log g$  that could be made by Nieva & Przybilla (2012), cannot be repeated here. We note, however, that the supergiants closest to the Sun in the sample, HD 125288 and HD 164353, are consistent with the CAS values within the mutual uncertainties, but they show overall larger abundances. In particular the surface abundances of nitrogen show clear indication of mixing of the atmospheres with CN-processed material from the stellar cores.

#### 5.4. Signatures of mixing with CNO-processed material

Different physical mechanisms can lead to mixing of CNO-cycled matter from the stellar core to the surface of rotating stars. Examples are meridional circulation or shear mixing due to differential rotation (e.g. Maeder & Meynet 2012; Langer 2012) further modified by the presence of magnetic fields. As a consequence, ratios of the surface carbon, nitrogen, and oxygen mass fractions, and the helium mass fractions are expected to appear in relatively narrow regions in diagnostic diagrams (Przybilla et al. 2010; Maeder et al. 2014) as shown in Fig. 11. All ratios were normalised to the initial values so as to make the comparison to



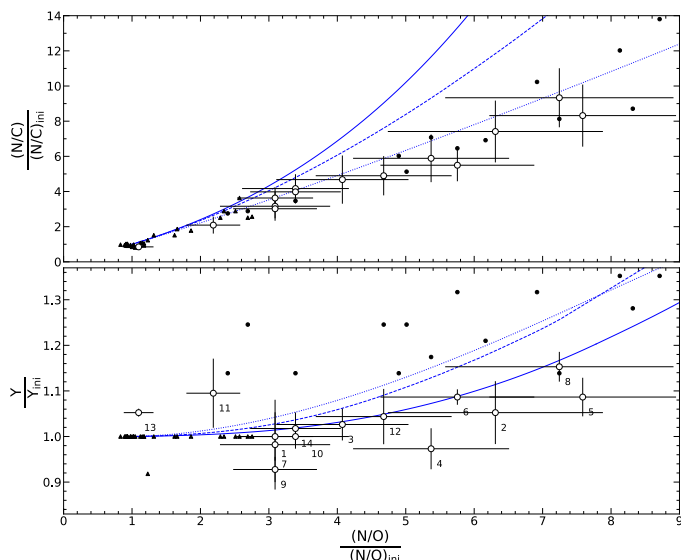


**Fig. 11.** Nitrogen-to-carbon ratio (upper panel) and helium abundance (lower panel) versus nitrogen-to-oxygen ratio, normalised to cosmic abundance standard values (Nieva & Przybilla 2012). Objects from the present work (open symbols), B-type main-sequence stars (Nieva & Przybilla 2012, black triangles), and BA-type supergiants (Przybilla et al. 2010, black dots) are compared to predictions from stellar evolution models. Solid lines:  $15 M_{\odot}$ ,  $\Omega_{\text{rot}} = 0.95 \Omega_{\text{crit}}$  model by Georgy et al. (2013); dashed lines:  $15 M_{\odot}$ ,  $\Omega_{\text{rot}} = 0.568 \Omega_{\text{crit}}$  model by Ekström et al. (2012); dotted lines:  $25 M_{\odot}$ ,  $\Omega_{\text{rot}} = 0.568 \Omega_{\text{crit}}$  model by Ekström et al. (2012). For all tracks, a metallicity of  $Z = 0.014$  was assumed. Abundances in the models were normalised with respect to their initial model values.

the evolution tracks easier – the observations were normalised relative to CAS abundances (see Table 6,  $Y_{\text{ini}} = 0.276$ ), the models to their respective (solar) initial values.

As the  $N/C$  versus  $N/O$  plot shows little dependence on the initial stellar masses, rotation velocities, and nature of the mixing processes up to relative enrichment of  $N/O$  by a factor of about four, it constitutes an ideal quality test for observational results (Maeder et al. 2014). The CNO signatures of the present sample supergiants closely follow both the path predicted by models and the observational data of Przybilla et al. (2010) and Nieva & Przybilla (2012). This gives confidence that systematic errors in the present atmospheric parameters are indeed small.

The star HD 159110 (ID#13) appears at CAS initial values for CNO abundances, while HD 119646 (ID#11) exhibits CNO abundances consistent with mixing signatures on the main sequence (i.e. relative enrichment of  $(N/O)/(N/O)_{\text{ini}} \lesssim 3$ ). The majority of the sample stars is noticeably enriched in CN-processed matter, with enhancement almost reaching the high values observed for some of the more evolved BA-type supergiants.

For most of the analysed objects, helium abundances are slightly lower than predicted by the models while being consistent with the initial helium abundance within the  $1\sigma$  uncertainties. Three of the sample objects (ID#9, #11, and in particular #13) deviate somewhat from this value while they are expected to show no modification. This is true when only statistical uncertainties are considered, which are displayed in Fig. 11. However, potential systematic errors also need to be considered and we emphasise that the offset of ID#13 from the initial value corresponds to only 0.02 dex. Such differences are much smaller than the symbol sizes in the upper panel of Fig. 11, stressing the enor-

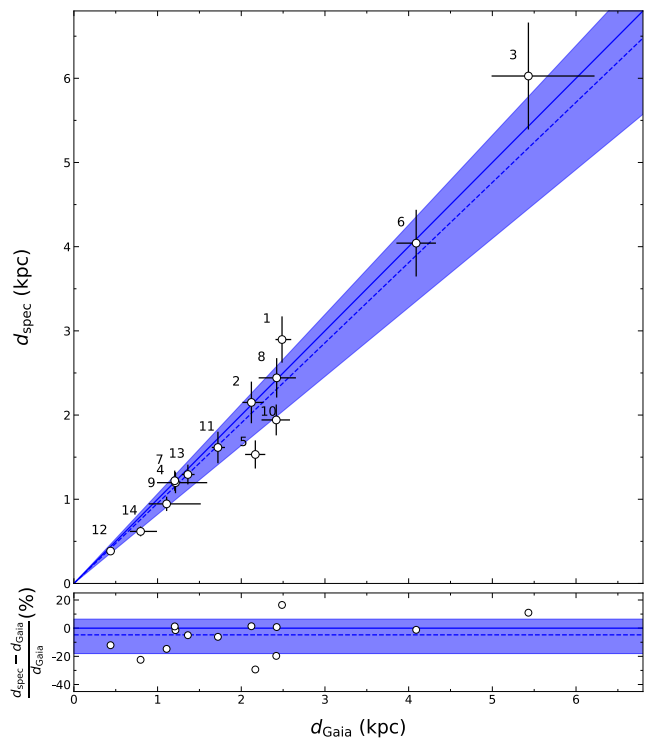


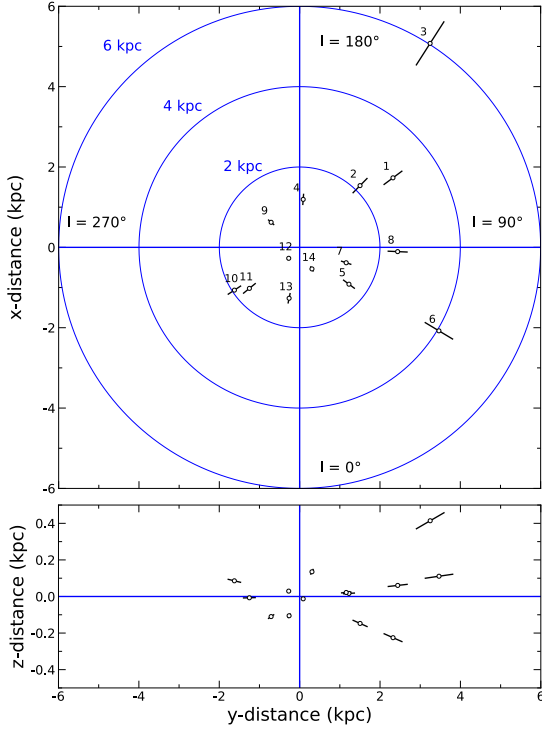
**Fig. 12.** Comparison of spectroscopic distances derived in the present work and distances based on Gaia EDR3 parallaxes (upper) and their relative differences (lower panel). The solid blue lines depict equivalence, while the dashed lines show the best linear fit to the data. The shaded area marks the region of  $1\sigma$  standard deviation from the mean.

mous changes in mostly nitrogen (and to a lesser extent carbon and oxygen) abundances versus the enrichment of helium which is difficult to determine. The highest helium enrichment found in our sample stars is about 15% above the initial value. This is different to the BA-type supergiants, which show larger enhancement values. We note that different helium lines were analysed by Przybilla et al. (2010), as many of the stars are cooler than the present sample stars. However, an investigation of the cause of these differences is beyond the scope of the present paper.

### 5.5. Spectroscopic distances

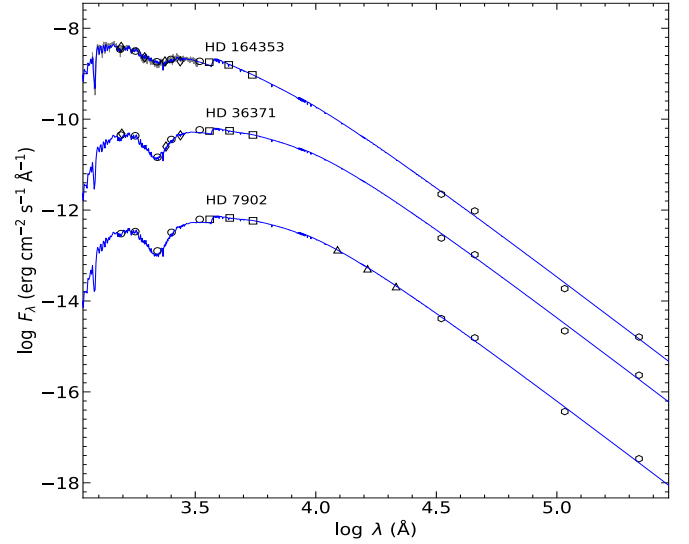
The spectroscopic distances derived in this work depend on several parameters deduced both from the quantitative spectral analysis and inferred from fundamental parameters on the basis of stellar evolution models, spectral synthesis codes, and photometric data (see Eqn. 3). As already mentioned in brief in Sect. 4.4, the comparison with independent distance estimations (e.g. Gaia EDR3) can provide valuable insight into systematic problems in the derivation of important parameters for the entire sample. It can, however, also highlight individual sample objects that may have undergone exceptional evolutionary pathways. Binarity (with and without associated mass transfer) and post-asymptotic giant branch evolutionary histories can leave signatures detectable in this approach. Regardless as to whether the star has evolved 'normally' or not, it may be stated that the primary sources of uncertainty are evolutionary mass  $M_{\text{evol}}$  and surface gravity  $\log g$ , so that potential offsets in distances most probably stem from systematically biased parameters.

Figure 12 shows a direct comparison (upper panel) and relative difference (lower panel) of our spectroscopic distances  $d_{\text{spec}}$  and distances  $d_{\text{Gaia}}$  derived from Gaia EDR3 parallaxes. Specif-



**Fig. 13.** Distribution of sample stars in the Galactic plane (upper) and elevation above the plane (lower panel) based on spectroscopic distances in Cartesian coordinates with the Sun at the origin. The Galactic centre lies towards the bottom in the upper panel, at Galactic longitude  $0^\circ$ . Blue circles enclose regions of equal distance from the Sun, as indicated.

ically,  $d_{\text{Gaia}}$  is the ‘photogeometric’ Bayesian estimation of distance by Bailer-Jones et al. (2021), which in addition to Gaia EDR3 parallaxes also takes into account the objects colour and apparent magnitude to achieve yet higher accuracy. In the direct comparison, we see a good agreement of the two distance determinations for the individual objects. The relative differences display a small mean offset of  $\mu_s = -6\%$  with a sample standard deviation of  $\sigma_s = 12\%$ , showing the excellent agreement between the distances. Even though most objects lie within about 2.5 kpc from the Sun, the relationship does not seem to degrade noticeably at larger distances, as can be seen for the cases of HD 184943 (ID #6,  $d_{\text{spec}} = 4$  kpc) and HD 25914 (ID #3,  $d_{\text{spec}} = 6$  kpc). Two of our sample stars, HD 7902 (ID #1) and HD 183143 (ID #5), depart somewhat from the mean relationship. While we cannot offer a robust explanation for the discrepancy in distance of either of these objects, we note that both are evolved stars towards the upper mass limit of our sample. Small scale systematic errors in mass estimates, as discussed in Sect. 4.2, are maximised in this region. For ID#1 a mass reduced by  $1 M_\odot$  would be sufficient to reach agreement within the mutual  $1\sigma$ -uncertainties of the two distances. Maximum systematic effects would be needed for ID#5 in this picture, requiring an initially non-rotating single star, but at the same time it is one of the two stars with the largest CNO mixing signature in the sample. This could possibly be interpreted in terms of a binary history. However, a further discussion of this is not warranted by the information available. Considering the offset  $\mu_s$  of the relative differences is of the order of  $-0.5\sigma_s$ , we may conclude that the line of regression is compatible with an offset of zero. It may on the other hand reflect some unaccounted low-scale systematics, which, however, have no significant impact on the basic conclusions of the present work.



**Fig. 14.** Examples of spectral energy distributions of sample stars. ATLAS9-SEDs, normalised in  $V$  and reddened according to values from Table 5 (blue lines) are compared to IUE spectrophotometry (grey lines) and photometric data in various wavelength bands: ANS (circles), TD1 (diamonds), Johnson (squares), 2MASS (triangles), and ALLWISE data (hexagons). Data with bad quality flags were removed. For better visibility, the SEDs and photometry of HD 164353 and HD 7902 were shifted by +1 and  $-1$  dex, respectively.

The distribution of the sample stars in the Galactic disk is depicted in Fig. 13. The sample objects span Galactocentric distances in the range of  $R_g = 7$ –13 kpc (calculated for a distance of the Sun to the Galactic centre of 8.178 kpc, Gravity Collaboration et al. 2019), while the range of elevations above and below the Galactic plane is fairly small, typically within 200 pc. Only our outermost supergiant, HD 25914 (ID#3), is located  $\sim 0.4$  kpc above the Galactic plane. While the arrangement of the objects along the spiral arms is not immediately obvious, a closer inspection using the spiral arm delineation by Xu et al. (2021) shows that stars with IDs #10, 11, and 13 are located in the Carina-Sagittarius Arm, #6, 7, 8, 9, 12, and 14 in the Local Arm, #1, 2, and 4 are associated with the Perseus Arm and #3 is situated in the Outer Arm. Star #5 lies in the Sagittarius-Carina arm if  $d_{\text{Gaia}}$  is adopted, and otherwise between that and the Local Arm if  $d_{\text{spec}}$  is considered.

### 5.6. Sight lines – reddening law

For the high-precision determination of the interstellar sight lines to the sample objects, the model ATLAS9-SEDs were fitted to photometric observations in various bands as well as to UV spectrophotometry from the IUE-satellite. Figure 14 exemplarily summarises the result of this fitting process for three out of the 14 sample stars to give an impression of the quality of the fits, ordered from top to bottom by increasing values of colour excess  $E(B - V)$ . For most objects sufficient constraining observations were suitable for comparison and resulted in very small associated uncertainties in both  $R_V$  and  $E(B - V)$ . Values for  $R_V$  vary between 2.9 and 3.6, mostly concentrating around the typical ISM value of 3.1, and reddening values vary typically between 0.1 and 0.8, see Table 5 for a summary of the results. The peculiar case of HD 183143 was already briefly discussed in Sect. 4.3.

### 5.7. Evolutionary status

The evolutionary status of the sample stars can be derived by comparison to stellar evolution tracks. Two complementary diagnostic diagrams may be employed for this, the spectroscopic HRD (sHRD,  $\log(\mathcal{L}/\mathcal{L}_\odot)$  versus  $\log T_{\text{eff}}$ , introduced by Langer & Kudritzki 2014) and the HRD ( $\log L/L_\odot$  versus  $\log T_{\text{eff}}$ ). The sHRD is based only on observed atmospheric parameters (like the Kiel diagram –  $\log g$  versus  $\log T_{\text{eff}}$  –, not shown here), while the HRD requires knowledge of the distance and corrections for interstellar extinction to be taken into account. Both were derived in the present work and we give preference to spectroscopic distances. The positions of the sample stars in both diagrams with respect to evolutionary tracks for rotating stars by Ekström et al. (2012) are shown in Fig. 15. We note the very similar positions of the sample stars relative to the evolution tracks. This is consistent with them likely being post-main-sequence objects with ZAMS masses between about 9 to 30  $M_\odot$  on the first crossing of the HRD towards the red supergiant phase (star #13 is a potential exception, it may alternatively be in the last stages of core H-burning, depending on its detailed properties). They are located on the cool side of the bi-stability jump for stellar winds (e.g. Lamers et al. 1995) and are slowly rotating, with  $v \sin i$  in the range of about 20 to 50  $\text{km s}^{-1}$ , as expected for such B-type supergiants (see e.g. Vink et al. 2010). Evolutionary ages vary between about 7 Myr for the most massive to about 29 Myr for the least massive sample objects, as inferred from isochrones indicated in the upper panel of Fig. 15. We emphasise again that the masses and ages are derived assuming that the particular rotation rates in evolution models and isochrones are representative on average for the sample. Systematic shifts in mass and age result if the initial rotational velocities had other values, but we expect them to be covered by our uncertainties in most cases.

We note that the sample stars show a variety of metallicities (see Table 6) because of their different positions in the Galactic disk. The most metal-poor star in the present work is HD 25914 at  $Z = 0.010$  in the Outer Arm, while several objects reach super-CAS metallicities in the inner Milky Way, up to  $Z = 0.019$ , that is the variations reach up to about 30% below and 40% above the CAS value. Moreover, the chemical composition of the sample stars varies from (scaled) solar, as implemented by Ekström et al. (2012) for the  $Z = 0.014$  models, to the bracketing analogous  $Z = 0.006$  (Eggenberger et al. 2021) and  $Z = 0.020$  models (Yusof et al. 2022). The net effects are a more efficient transport of angular momentum and CNO-processed material with decreasing metallicity and a higher mass-loss with increasing metallicity. However, we do not see the resulting differences as critical for the present work in terms of parameters deduced from the comparison such as ZAMS or evolutionary masses. The evolutionary tracks remain similar throughout the metallicity range (see e.g. Yusof et al. 2022, their Fig. 5), such that the resulting systematics are expected to lie within our uncertainties.

The number of sample stars is too low to investigate the effects responsible for the mixing of the surface layers with CNO-processed material from the core systematically. Two findings are in line with the general picture of rotational mixing: the two stars with CNO signatures closest to the pristine values (#11, #13) are closest to the terminal-age main sequence, towards lower masses, and the stars showing the highest processing (#5 and #8) are the most evolved (i.e. showing the coolest temperatures) and tend to be among the most massive sample stars. On the other hand, star #3 – the most massive and most metal-poor object of the sample – shows only a milder degree of chemical mixing, which may be the consequence of an initially slower

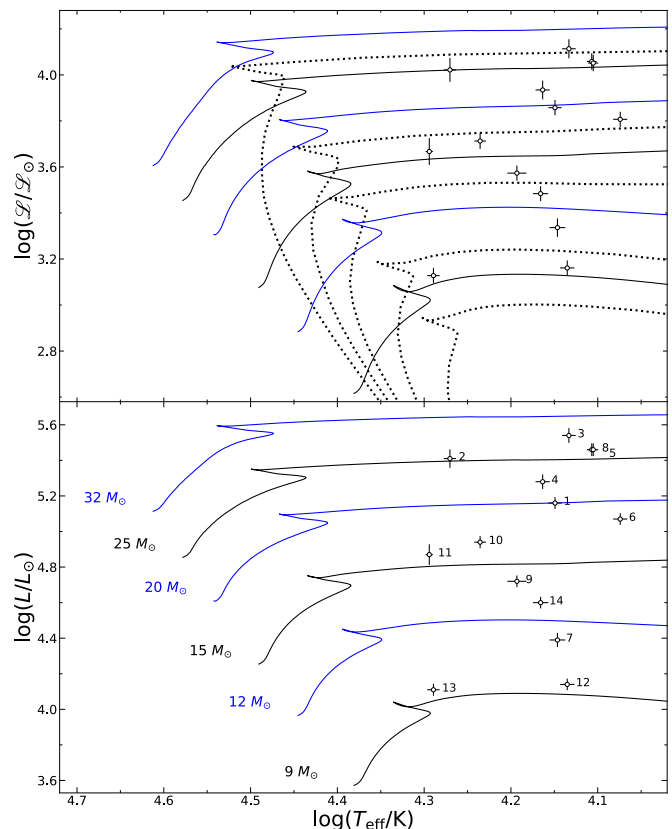
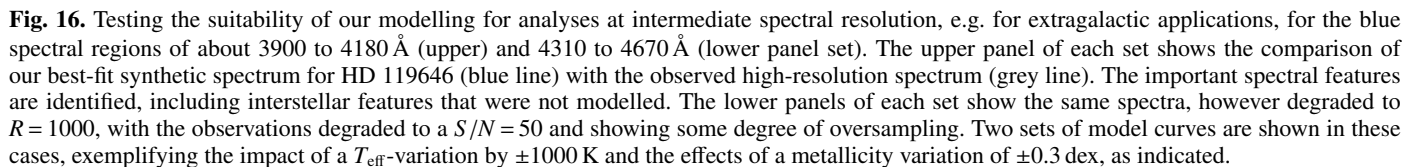


**Fig. 15.** Location of the sample objects in two diagnostic diagrams compared to the loci of evolution tracks for stars rotating with  $\Omega_{\text{rot}} = 0.568 \Omega_{\text{crit}}$  by Ekström et al. (2012), for various ZAMS-masses as indicated. Isochrones for the model grid, corresponding to ages of  $\log \tau_{\text{evol}} \in \{6.85, 7.05, 7.20, 7.40, 7.60\}$  are depicted as dotted lines in the upper panel (increasing in age from top to bottom). Upper panel: sHRD; lower panel: HRD.  $1\sigma$  error bars are indicated.

rotation than average. The issue has to be revisited based on a much larger sample of objects.

## 6. Test for extragalactic applications at intermediate spectral resolution

High-resolution spectroscopy of B-type supergiants as presented here can be conducted in galaxies beyond the Magellanic Clouds only at the cost of long exposure times of the order of hours on large telescopes (e.g. Urbaneja et al. 2011). Fortunately, many of the stronger diagnostic lines are isolated, so that intermediate-resolution spectroscopy ( $R \simeq 1000\text{--}5000$ ) suffices to allow quantitative analyses, at the loss of only the weaker spectral lines. This also opens up the possibility of employing multi-object spectroscopy, in particular when investigating galaxies beyond the Local Group, providing multiplexing of the order a few tens to hundreds of objects to be observed simultaneously. This comprises various successful techniques that have been implemented already as multi-slit spectroscopy (e.g. with the FOCAL Reducer/low dispersion Spectrograph 2, FORS2, on the ESO Very Large Telescope VLT, e.g. Kudritzki et al. 2016), multi-fibre spectroscopy (with the Large Sky Area Multi-Object Fibre Spectroscopic Telescope, LAMOST, e.g. Liu et al. 2022) or integral-field spectroscopy (as with the Multi Unit Spectroscopic Explorer, MUSE, on the VLT, e.g. González-Torà et al. 2022).



however for an artificially downgraded  $R = 1000$  reachable with FORS2, is shown in the lower subpanels, where a  $S/N = 50$  is simulated for the observation. Excellent agreement is achieved in both cases, except for some small details. Moreover, modified models by  $\pm 1000$  K in  $T_{\text{eff}}$  and  $\pm 0.3$  dex in metal abundances are also shown in the intermediate-resolution case. This shows that a simultaneous evaluation of all the spectral features, both the atmospheric parameters ( $\log g$  is constrained by the response of the Balmer lines, not shown here) as well as the elemental abundances can be performed using  $\chi^2$  minimisation tech-



niques in the multi-parameter space, with uncertainties that are only slightly larger than in the high-resolution case:  $\Delta T_{\text{eff}}$  in the range of about 300-1000 K,  $\Delta \log g$  of about 0.10 dex, and elemental abundances in the range of about 0.10 to 0.15 dex. We note in particular that the ionisation equilibria Si II/III(IV), and in the case that red wavelengths are also covered O I/II, remain available at intermediate resolution. The microturbulent velocity can best be constrained from the rather numerous Si II/III and O I/II lines (in contrast to the minimalistic approach of concentrating only on the Si III triplet 4552-4574 Å, e.g. Hunter et al. 2007).

We conclude that the present hybrid non-LTE spectrum synthesis technique based on reliable model atoms allows for comprehensive quantitative analyses of B-type supergiants on the basis of intermediate-resolution spectra. This opens up the prospect of B-type supergiants as versatile tools to address a number of highly-relevant astrophysical topics in the context of extragalactic stellar astronomy.

Even with available instrumentation on the current generation of 8-10m telescopes, a wide range of detailed studies, in particular concerning galactic evolution (galactic abundance gradients, the galaxy mass-metallicity relationship, e.g. Urbaneja et al. 2005a; Kudritzki et al. 2012, 2014; Castro et al. 2012) and the cosmic distance scale (via application of the FGLR, e.g. Urbaneja et al. 2017), can be addressed by investigating supergiants in galaxies in the field and in the nearby galaxy groups. With the advent of the Extremely Large Telescopes (ELTs), the step to investigate supergiants in galaxies in the nearby Virgo and Fornax galaxy clusters will become feasible, allowing environmental effects to be studied. However, as adaptive optics techniques will be required to reach the full potential of the ELTs in terms of spatial resolution, spectroscopic observations will have to concentrate on redder wavelength regions, at least initially. For example, the High Angular Resolution Monolithic Optical and Near-infrared Integral field spectrograph (HARMONI, Thatte et al. 2021) on the ESO ELT will cover wavelengths beyond 4700 Å and the multi-object spectrograph MOSAIC (Hammer et al. 2021) beyond 4500 Å. The information content will be lower than at bluer wavelengths, but suitable spectral lines for analyses are present, see the figures in Appendix A. Important for the scientific return will be to achieve wide wavelength coverage.

## 7. Summary and conclusions

A hybrid non-LTE spectrum synthesis approach for quantitative analyses of luminous B-type supergiants with masses up to about  $30 M_{\odot}$  was presented, where most spectral lines are formed in a photosphere that is not significantly affected by the stellar wind. It was shown that practically the entire observed optical to near-IR high-resolution spectra can be reliably reproduced, including the dozen chemical elements with the highest abundances. The modelling was thoroughly tested for 14 sample objects spanning a  $T_{\text{eff}}$ -range from about 12 000 to 20 000 K (i.e. spectral types B8 to B1.5) and luminosity classes II, Ib, Iab, and Ia. The present work helps to connect the region of late O- and early B-type stars on the main-sequence with luminosity classes V to III (Nieva & Przybilla 2012, 2014) and the cooler BA-type supergiants (Przybilla et al. 2006a; Farnstein & Przybilla 2012), which will allow stellar evolution to be tracked observationally throughout the hot regime of the HRD in a homogeneous manner.

Due to the highly interactive and iterative nature of the approach, the time required to carry out the analysis procedure for

a comprehensive solution of one sample object amounts to typically 2 weeks for experienced users. For a demonstration of the applicability of a method and a first application, this is an acceptable time investment. But, obviously, a combination of the models with faster, more automatised state-of-the-art analysis techniques (see e.g. Sect. 3.8 of Simón-Díaz 2020) is required for future larger-scale applications.

It has been shown that the atmospheric parameters of B-type supergiants can be determined with high precision and accuracy using the hybrid non-LTE approach. The effects of turbulent pressure were taken into account for the first time for B-type supergiants, and they lead to (small) systematic shifts in the atmospheric parameters. Effective temperatures can be constrained to 2-3% uncertainty, surface gravities to better than 0.07 dex uncertainty, and elemental abundances with uncertainties of 0.05 to 0.10 dex (statistical  $1\sigma$ -scatter) and about 0.1 dex (systematic error). Classical LTE analyses that can be partly successful for the analysis of main-sequence stars at similar  $T_{\text{eff}}$  cannot be expected to yield any meaningful results for supergiant analyses (Fig. 4 gives an impression of the differences).

Precise and accurate atmospheric parameters also allow an improved characterisation of the interstellar reddening and the reddening law along the sight lines towards the supergiants to be made. The importance of B-type supergiants in this context lies in their large luminosities, so that sight lines to very distant parts of the Milky Way may become traceable in the era of large spectroscopic surveys (e.g. Xiang et al. 2022). A comparison with stellar evolution models then also allows the fundamental parameters to be determined. In particular future Gaia data releases will help to further reduce the uncertainties for Galactic supergiants by providing stronger astro- and photometric constraints to cross-check resulting spectroscopic solutions.

Most of the sample stars show signatures of the surface layers having experienced (rotational) mixing with CNO-processed material from the core, and the positions of the stars in the HRD are consistent with hydrogen shell-burning being active but core He-burning probably having not yet ignited (which happens for the investigated mass range earliest at  $\log T_{\text{eff}} \simeq 4.1$ , and cooler, according to the models of Ekström et al. 2012). Unlike main-sequence early B-type stars in the solar neighbourhood (Nieva & Przybilla 2012), the B-supergiant sample does not show chemical homogeneity for the heavier elements. However, this is not unexpected, as the objects cover a wider range of Galactocentric distances, that is they will be subject to Galactic abundance gradients (e.g. Méndez-Delgado et al. 2022).

Finally, it was shown that the full spectrum synthesis approach makes applications to intermediate-resolution spectra possible, with only slightly increased error margins. Extragalactic samples of B- and A-type supergiants below the  $\sim 30 M_{\odot}$  limit can therefore be analysed homogeneously in the future. A major step for such applications will be reached once multi-object spectrographs on ELTs become available. Quantitative spectroscopy of supergiants in the star-forming galaxies of the Virgo and Fornax galaxy clusters can then commence, allowing galaxy evolution in the different environments to be studied – in the field, in groups, and in clusters – in more detail than currently feasible on the basis of gaseous nebulae.

*Acknowledgements.* D.W. and N.P. gratefully acknowledge support from the Austrian Science Fund FWF project DK-ALM, grant W1259-N27. Based on data obtained from the ESO Science Archive Facility with DOI(s): <https://doi.org/10.18727/archive/24>. Based on observations collected at the Centro Astronómico Hispano Alemán at Calar Alto (CAHA), operated jointly by the Max-Planck Institut für Astronomie and the Instituto de Astrofísica de Andalucía (CSIC), proposals H2001-2.2-011 and H2005-2.2-016. Travel of N.P. to the Calar Alto Observatory was supported by the Deutsche Forschungsges-

meinschaft (DFG) under grant PR 685/1-1. The latter observational data are available under <https://doi.org/10.5281/zenodo.6802567>. We are grateful to A. Irrgang for several updates of DETAIL and SURFACE. We thank the referee for useful suggestions to improve on the clarity of the paper. This work has made use of data from the European Space Agency (ESA) mission *Gaia* (<https://www.cosmos.esa.int/gaia>), processed by the *Gaia* Data Processing and Analysis Consortium (DPAC, <https://www.cosmos.esa.int/web/gaia/dpac/consortium>). Funding for the DPAC has been provided by national institutions, in particular the institutions participating in the *Gaia* Multilateral Agreement. This publication makes use of data products from the Two Micron All Sky Survey, which is a joint project of the University of Massachusetts and the Infrared Processing and Analysis Center/California Institute of Technology, funded by the National Aeronautics and Space Administration and the National Science Foundation. This publication makes use of data products from the Wide-field Infrared Survey Explorer, which is a joint project of the University of California, Los Angeles, and the Jet Propulsion Laboratory/California Institute of Technology, funded by the National Aeronautics and Space Administration. This research has made use of the SVO Filter Profile Service (<http://svo2.cab.inta-csic.es/theory/fps/>) supported from the Spanish MINECO through grant AYA2017-84089.

## References

- Allen, C. W. 1973, *Astrophysical quantities*, 3rd edn. (Athlone Press, London)
- Bailer-Jones, C. A. L., Rybizki, J., Fouesneau, M., Demleitner, M., & Andrae, R. 2021, *AJ*, 161, 147
- Becker, S. R. 1998, *ASP Conf. Ser.*, 131, 137
- Berger, T. A., Kudritzki, R. P., Urbaneja, M. A., et al. 2018, *ApJ*, 860, 130
- Bessell, M. S., Castelli, F., & Plez, B. 1998, *A&A*, 333, 231
- Bresolin, F., Gieren, W., Kudritzki, R. P., Pietrzyński, G., & Przybilla, N. 2002, *ApJ*, 567, 277
- Bresolin, F., Kudritzki, R. P., Urbaneja, M. A., et al. 2016, *ApJ*, 830, 64
- Bresolin, F., Pietrzyński, G., Gieren, W., et al. 2004, *ApJ*, 600, 182
- Bresolin, F., Pietrzyński, G., Urbaneja, M. A., et al. 2006, *ApJ*, 648, 1007
- Bresolin, F., Urbaneja, M. A., Gieren, W., Pietrzyński, G., & Kudritzki, R. P. 2007, *ApJ*, 671, 2028
- Brott, I., de Mink, S. E., Cantiello, M., et al. 2011, *A&A*, 530, A115
- Butler, K. & Giddings, J. R. 1985, *Newsletter of Analysis of Astronomical Spectra*, 9 (Univ. London)
- Castro, N., Fossati, L., Langer, N., et al. 2014, *A&A*, 570, L13
- Castro, N., Urbaneja, M. A., Herrero, A., et al. 2012, *A&A*, 542, A79
- Cayrel, R. 1958, *Annales d'Astrophysique*, Suppl., 6, 5
- Clark, J. S., Najarro, F., Negueruela, I., et al. 2012, *A&A*, 541, A145
- Cordiner, M. A., Cox, N. L. J., Evans, C. J., et al. 2011, *ApJ*, 726, 39
- Cordiner, M. A., Cox, N. L. J., Trundle, C., et al. 2008, *A&A*, 480, L13
- Cox, N. L. J., Cami, J., Farhang, A., et al. 2017, *A&A*, 606, A76
- Cox, N. L. J., Cordiner, M. A., Cami, J., et al. 2006, *A&A*, 447, 991
- Cox, N. L. J., Cordiner, M. A., Ehrenfreund, P., et al. 2007, *A&A*, 470, 941
- Crowther, P. A., Lennon, D. J., & Walborn, N. R. 2006, *A&A*, 446, 279
- Cutri, R. M., Wright, E. L., Conrow, T., et al. 2021, *VizieR Online Data Catalog*, II/328
- Dufton, P. L. 1972, *A&A*, 16, 301
- Dufton, P. L. 1979, *A&A*, 73, 203
- Dufton, P. L., Ryans, R. S. I., Trundle, C., et al. 2005, *A&A*, 434, 1125
- Ebenbichler, A., Postel, A., Przybilla, N., et al. 2022, *A&A*, 662, A81
- Eggenberger, P., Ekström, S., Georgy, C., et al. 2021, *A&A*, 652, A137
- Ekström, S., Georgy, C., Eggenberger, P., et al. 2012, *A&A*, 537, A146
- Evans, C. J., Bresolin, F., Urbaneja, M. A., et al. 2007, *ApJ*, 659, 1198
- Firnstein, M. & Przybilla, N. 2012, *A&A*, 543, A80
- Fitzpatrick, E. L. 1999, *PASP*, 111, 63
- Fraser, M., Dufton, P. L., Hunter, I., & Ryans, R. S. I. 2010, *MNRAS*, 404, 1306
- Froese Fischer, C. & Tachiev, G. 2004, *At. Data and Nucl. Data Tables*, 87, 1
- Froese Fischer, C., Tachiev, G., & Irimia, A. 2006, *At. Data and Nucl. Data Tables*, 92, 607
- Gaia Collaboration, Brown, A. G. A., Vallenari, A., et al. 2021, *A&A*, 649, A1
- Gaia Collaboration, Prusti, T., de Bruijne, J. H. J., et al. 2016, *A&A*, 595, A1
- Georgy, C., Ekström, S., Granada, A., et al. 2013, *A&A*, 553, A24
- Giddings, J. R. 1981, PhD thesis, (Univ. London)
- González-Torà, G., Urbaneja, M. A., Przybilla, N., et al. 2022, *A&A*, 658, A117
- Gräfener, G., Koesterke, L., & Hamann, W. R. 2002, *A&A*, 387, 244
- Gravity Collaboration, Abuter, R., Amorim, A., et al. 2019, *A&A*, 625, L10
- Gray, D. F. 1975, *ApJ*, 202, 148
- Gray, R. O. & Corbally, C. J. 2009, *Stellar Spectral Classification* (Princeton: Princeton University Press)
- Grevesse, N. & Sauval, A. J. 1998, *Space Sci. Rev.*, 85, 161
- Hammer, F., Morris, S., Cuby, J. G., et al. 2021, *The Messenger*, 182, 33
- Haucke, M., Cidale, L. S., Venero, R. O. J., et al. 2018, *A&A*, 614, A91
- Heber, U., Hunger, K., Jonas, G., & Kudritzki, R. P. 1984, *A&A*, 130, 119
- Herrero, A., Berlanas, S. R., Gil de Paz, A., et al. 2022, *MNRAS*, 511, 3113
- Hillier, D. J. & Miller, D. L. 1998, *ApJ*, 496, 407
- Hirsch, H. A. 2009, PhD thesis, (Univ. Erlangen-Nürnberg)
- Hirschi, R., Meynet, G., & Maeder, A. 2004, *A&A*, 425, 649
- Hosek, Matthew W., J., Kudritzki, R. P., Bresolin, F., et al. 2014, *ApJ*, 785, 151
- Hubeny, I. 1988, *Comput. Phys. Commun.*, 52, 103
- Hubeny, I., Hummer, D. G., & Lanz, T. 1994, *A&A*, 282, 151
- Hubeny, I. & Lanz, T. 1995, *ApJ*, 439, 875
- Hummer, D. G. & Mihalas, D. 1988, *ApJ*, 331, 794
- Humphreys, R. M. 1978, *ApJS*, 38, 309
- Humphreys, R. M. & Davidson, K. 1979, *ApJ*, 232, 409
- Hunter, I., Brott, I., Langer, N., et al. 2009, *A&A*, 496, 841
- Hunter, I., Dufton, P. L., Smartt, S. J., et al. 2007, *A&A*, 466, 277
- Irrgang, A., Przybilla, N., Heber, U., et al. 2014, *A&A*, 565, A63
- Kaufer, A., Stahl, O., Tubbesing, S., et al. 1999, *The Messenger*, 95, 8
- Kimeswenger, S., Rainer, M., Przybilla, N., & Kausch, W. 2021, *AJ*, 161, 66
- Korn, A. J. 2002, in *Scientific Drivers for ESO Future VLT/VLTI Instrumentation*, ed. J. Bergeron & G. Monnet (Berlin: Springer), 199
- Kudritzki, R. P., Bresolin, F., & Przybilla, N. 2003, *ApJ*, 582, L83
- Kudritzki, R. P., Castro, N., Urbaneja, M. A., et al. 2016, *ApJ*, 829, 70
- Kudritzki, R. P., Puls, J., Lennon, D. J., et al. 1999, *A&A*, 350, 970
- Kudritzki, R. P., Urbaneja, M. A., Bresolin, F., Hosek, Matthew W., J., & Przybilla, N. 2014, *ApJ*, 788, 56
- Kudritzki, R. P., Urbaneja, M. A., Bresolin, F., et al. 2008, *ApJ*, 681, 269
- Kudritzki, R. P., Urbaneja, M. A., Gazak, Z., et al. 2012, *ApJ*, 747, 15
- Kupfer, T., Przybilla, N., Heber, U., et al. 2017, *MNRAS*, 471, 877
- Kurucz, R. 1993, CD-ROM No. 13 (Cambridge, Mass.: SAO)
- Kurucz, R. L. 2005, *Mem. Societa Astronomica Italiana Suppl.*, 8, 14
- Lamers, H. J. G. L. M., Snow, T. P., & Lindholm, D. M. 1995, *ApJ*, 455, 269
- Langer, N. 2012, *ARA&A*, 50, 107
- Langer, N. & Kudritzki, R. P. 2014, *A&A*, 564, A52
- Lanz, T. & Hubeny, I. 2007, *ApJS*, 169, 83
- Lee, J. K., Rolleston, W. R. J., Dufton, P. L., & Ryans, R. S. I. 2005, *A&A*, 429, 1025
- Lefever, K., Puls, J., & Aerts, C. 2007, *A&A*, 463, 1093
- Lennon, D. J., Dufton, P. L., & Fitzsimmons, A. 1992, *A&AS*, 94, 569
- Lennon, D. J., Dufton, P. L., & Fitzsimmons, A. 1993, *A&AS*, 97, 559
- Lequeux, J., Peimbert, M., Rayo, J. F., Serrano, A., & Torres-Peimbert, S. 1979, *A&A*, 500, 145
- Limongi, M. & Chieffi, A. 2018, *ApJS*, 237, 13
- Liu, C., Kudritzki, R. P., Zhao, G., et al. 2022, *ApJ*, 932, 29
- Maeder, A. & Meynet, G. 2001, *A&A*, 373, 555
- Maeder, A. & Meynet, G. 2012, *Rev. Mod. Phys.*, 84, 25
- Maeder, A., Przybilla, N., Nieva, M. F., et al. 2014, *A&A*, 565, A39
- Maoloino, R., Nagao, T., Grazian, A., et al. 2008, *A&A*, 488, 463
- Mao, J., Badnell, N. R., & Del Zanna, G. 2020, *A&A*, 643, A95
- Markova, N. & Puls, J. 2008, *A&A*, 478, 823
- Martin, W. C., Kaufman, V., & Musgrove, A. 1993, *J. Phys. Chem. Ref. Data*, 22, 1179
- Matteucci, F. 2008, in *Massive Stars as Cosmic Engines*, ed. F. Bresolin, P. A. Crowther, & J. Puls, Vol. 250 (Cambridge University Press, Cambridge), 391
- McErlean, N. D., Lennon, D. J., & Dufton, P. L. 1999, *A&A*, 349, 553
- McEvoy, C. M., Dufton, P. L., Evans, C. J., et al. 2015, *A&A*, 575, A70
- Méndez-Delgado, J. E., Amayo, A., Arellano-Córdova, K. Z., et al. 2022, *MNRAS*, 510, 4436
- Mermilliod, J. C. 1997, *VizieR Online Data Catalog*, 2168
- Morel, T. & Butler, K. 2008, *A&A*, 487, 307
- Morel, T., Butler, K., Aerts, C., Neiner, C., & Briquet, M. 2006, *A&A*, 457, 651
- Muschielok, B., Kudritzki, R. P., Appenzeller, I., et al. 1999, *A&A*, 352, L40
- Nelder, J. A. & Mead, R. 1965, *Comput. J.*, 7, 308
- Nieva, M. F. & Przybilla, N. 2006, *ApJ*, 639, L39
- Nieva, M. F. & Przybilla, N. 2008, *A&A*, 481, 199
- Nieva, M. F. & Przybilla, N. 2012, *A&A*, 539, A143
- Nieva, M. F. & Przybilla, N. 2014, *A&A*, 566, A7
- Nieva, M. F. & Simón-Díaz, S. 2011, *A&A*, 532, A2
- Pauldrach, A. W. A., Hoffmann, T. L., & Lennon, M. 2001, *A&A*, 375, 161
- Pfeiffer, M. J., Frank, C., Baumüller, D., Fuhrmann, K., & Gehren, T. 1998, *A&AS*, 130, 381
- Podsiadlowski, P. 1992, *PASP*, 104, 717
- Przybilla, N. 2005, *A&A*, 443, 293
- Przybilla, N. & Butler, K. 2001, *A&A*, 379, 955
- Przybilla, N. & Butler, K. 2004, *ApJ*, 609, 1181
- Przybilla, N., Butler, K., Becker, S. R., & Kudritzki, R. P. 2001a, *A&A*, 369, 1009
- Przybilla, N., Butler, K., Becker, S. R., & Kudritzki, R. P. 2006a, *A&A*, 445, 1099
- Przybilla, N., Butler, K., Becker, S. R., Kudritzki, R. P., & Venn, K. A. 2000, *A&A*, 359, 1085
- Przybilla, N., Butler, K., & Kudritzki, R. P. 2001b, *A&A*, 379, 936

- Przybilla, N., Farnstein, M., Nieva, M. F., Meynet, G., & Maeder, A. 2010, *A&A*, 517, A38
- Przybilla, N., Fossati, L., Hubrig, S., et al. 2016, *A&A*, 587, A7
- Przybilla, N., Fossati, L., & Jeffery, C. S. 2021, *A&A*, 654, A119
- Przybilla, N., Nieva, M. F., & Butler, K. 2008a, *ApJ*, 688, L103
- Przybilla, N., Nieva, M. F., & Butler, K. 2011, *J. Phys.: Conf. Ser.*, 328, 012015
- Przybilla, N., Nieva, M. F., & Edelmann, H. 2006b, *Baltic Astronomy*, 15, 107
- Przybilla, N., Nieva, M. F., Irrgang, A., & Butler, K. 2013, *EAS Publ. Ser.*, 63, 13
- Przybilla, N., Nieva, M. F., Tillich, A., et al. 2008b, *A&A*, 488, L51
- Puls, J., Kudritzki, R. P., Herrero, A., et al. 1996, *A&A*, 305, 171
- Puls, J., Urbaneja, M. A., Venero, R., et al. 2005, *A&A*, 435, 669
- Ramspeck, M., Heber, U., & Moehler, S. 2001, *A&A*, 378, 907
- Rodrigo, C. & Solano, E. 2020, in *Contributions to the XIV.0 Scientific Meeting (virtual) of the Spanish Astronomical Society*, 182
- Rodrigo, C., Solano, E., & Bayo, A. 2012, *SVO Filter Profile Service Version 1.0*, IVOA Working Draft 15 October 2012
- Ryans, R. S. I., Dufton, P. L., Rolleston, W. R. J., et al. 2002, *MNRAS*, 336, 577
- Rybicki, G. B. & Hummer, D. G. 1991, *A&A*, 245, 171
- Sana, H., de Mink, S. E., de Koter, A., et al. 2012, *Science*, 337, 444
- Santolaya-Rey, A. E., Puls, J., & Herrero, A. 1997, *A&A*, 323, 488
- Schafferoth, V., Casewell, S. L., Schneider, D., et al. 2021, *MNRAS*, 501, 3847
- Schiller, F. & Przybilla, N. 2008, *A&A*, 479, 849
- Searle, S. C., Prinja, R. K., Massa, D., & Ryans, R. 2008, *A&A*, 481, 777
- Seaton, M. J. 1962, in *Atomic and Molecular Processes*, ed. D. R. Bates (Academic Press, New York), 375
- Seaton, M. J., Yan, Y., Mihalas, D., & Pradhan, A. K. 1994, *MNRAS*, 266, 805
- Simón-Díaz, S. 2020, in *Reviews in Frontiers of Modern Astrophysics; From Space Debris to Cosmology*, ed. P. Kabath, D. Jones, & M. Skarka (Springer, Cham), 155
- Simón-Díaz, S., Godart, M., Castro, N., et al. 2017, *A&A*, 597, A22
- Simón-Díaz, S. & Herrero, A. 2007, *A&A*, 468, 1063
- Simón-Díaz, S. & Herrero, A. 2014, *A&A*, 562, A135
- Skrutskie, M. F., Cutri, R. M., Stiening, R., et al. 2006, *AJ*, 131, 1163
- Smartt, S. J., Crowther, P. A., Dufton, P. L., et al. 2001a, *MNRAS*, 325, 257
- Smartt, S. J., Venn, K. A., Dufton, P. L., et al. 2001b, *A&A*, 367, 86
- Szécsi, D., Agrawal, P., Wünsch, R., & Langer, N. 2022, *A&A*, 658, A125
- Tayal, S. S. 2007, *ApJS*, 171, 331
- Thatte, N., Tecza, M., Schnettler, H., et al. 2021, *The Messenger*, 182, 7
- Thompson, G. I., Nandy, K., Jamar, C., et al. 1995, *VizieR Online Data Catalog*, II/59B
- Tremonti, C. A., Heckman, T. M., Kauffmann, G., et al. 2004, *ApJ*, 613, 898
- Trundle, C., Dufton, P. L., Lennon, D. J., Smartt, S. J., & Urbaneja, M. A. 2002, *A&A*, 395, 519
- Trundle, C., Lennon, D. J., Puls, J., & Dufton, P. L. 2004, *A&A*, 417, 217
- U, V., Urbaneja, M. A., Kudritzki, R. P., et al. 2009, *ApJ*, 704, 1120
- Urbaneja, M. A., Herrero, A., Bresolin, F., et al. 2003, *ApJ*, 584, L73
- Urbaneja, M. A., Herrero, A., Bresolin, F., et al. 2005a, *ApJ*, 622, 862
- Urbaneja, M. A., Herrero, A., Kudritzki, R. P., et al. 2005b, *ApJ*, 635, 311
- Urbaneja, M. A., Herrero, A., Lennon, D. J., Corral, L. J., & Meynet, G. 2011, *ApJ*, 735, 39
- Urbaneja, M. A., Kudritzki, R. P., Bresolin, F., et al. 2008, *ApJ*, 684, 118
- Urbaneja, M. A., Kudritzki, R. P., Gieren, W., et al. 2017, *AJ*, 154, 102
- van Regemorter, H. 1962, *ApJ*, 136, 906
- Vink, J. S., Brott, I., Gräfener, G., et al. 2010, *A&A*, 512, L7
- Vrancken, M., Butler, K., & Becker, S. R. 1996, *A&A*, 311, 661
- Wesselius, P. R., van Duinen, R. J., de Jonge, A. R. W., et al. 1982, *A&AS*, 49, 427
- West, R. M., Lauberts, A., Jorgensen, H. E., & Schuster, H. E. 1987, *A&A*, 177, L1
- Wiese, W. L., Fuhr, J. R., & Deters, T. M. 1996, *J. Phys. & Chem. Ref. Data.*, Monograph 7 (AIP Press, Melville, NY)
- Xiang, M., Rix, H.-W., Ting, Y.-S., et al. 2022, *A&A*, 662, A66
- Xu, Y., Hou, L. G., Bian, S. B., et al. 2021, *A&A*, 645, L8
- Yusof, N., Hirschi, R., Eggenberger, P., et al. 2022, *MNRAS*, 511, 2814

## Appendix A: Example of a global model fit

The following figures show a comparison of the spectrum of HD 164353 as observed with FEROS and the best fitting global synthetic spectrum. The model was computed with the codes `ARLAS12/DETAIL/SURFACE` on basis of atmospheric parameters and elemental abundances for the star as summarised in Tables 5 and 6, respectively. The diagnostic stellar lines are identified in Figs. A.1 to A.8. A few interstellar ('IS') lines – the Ca H+K, Na D and K I resonance lines – and several diffuse interstellar bands (DIBs) are also identified, but they are missing in the model. Numerous sharp unmodelled features redwards of about 5870 Å are of telluric origin, due to H<sub>2</sub>O or from the O<sub>2</sub> A-, B- and γ-bands.



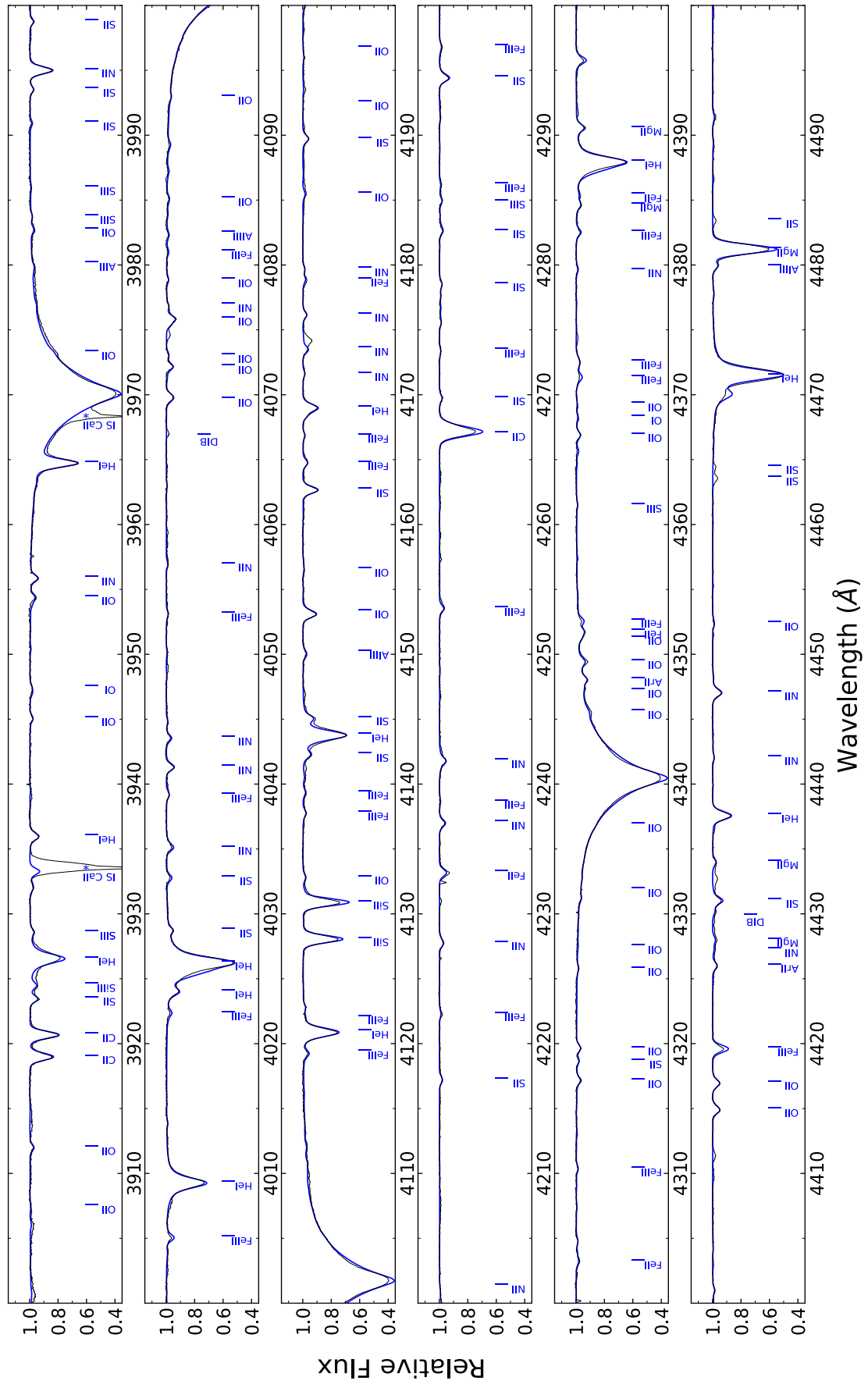


**Fig. A.1.** Comparison between the observed spectrum of HD 164353 (black) and the best fitting synthetic spectrum (blue) in the wavelength range of 3900 to 4500 Å.

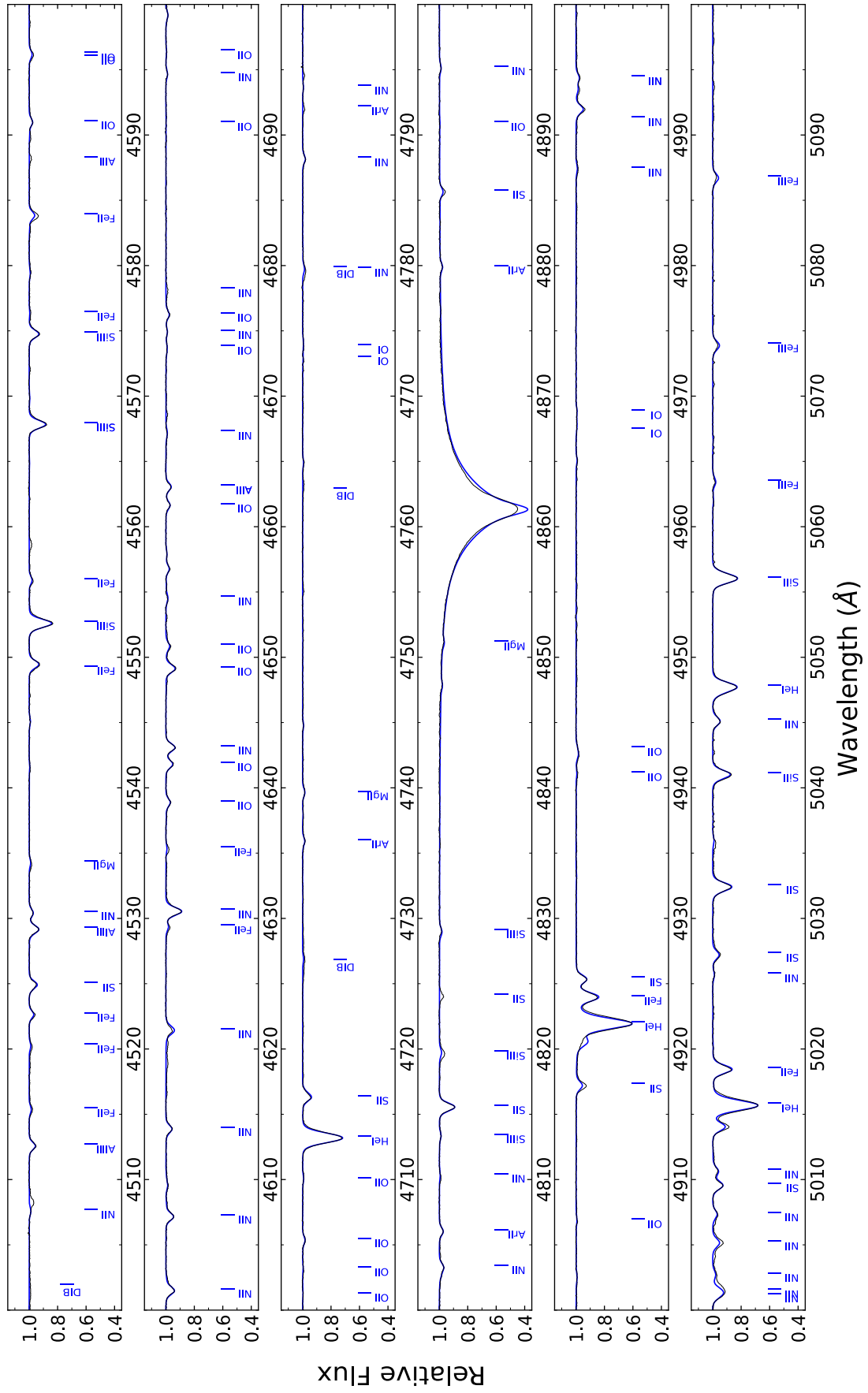


**Fig. A.2.** Same as Fig. A.1, but in the wavelength range  $\lambda\lambda 4500\text{--}5100$  Å.

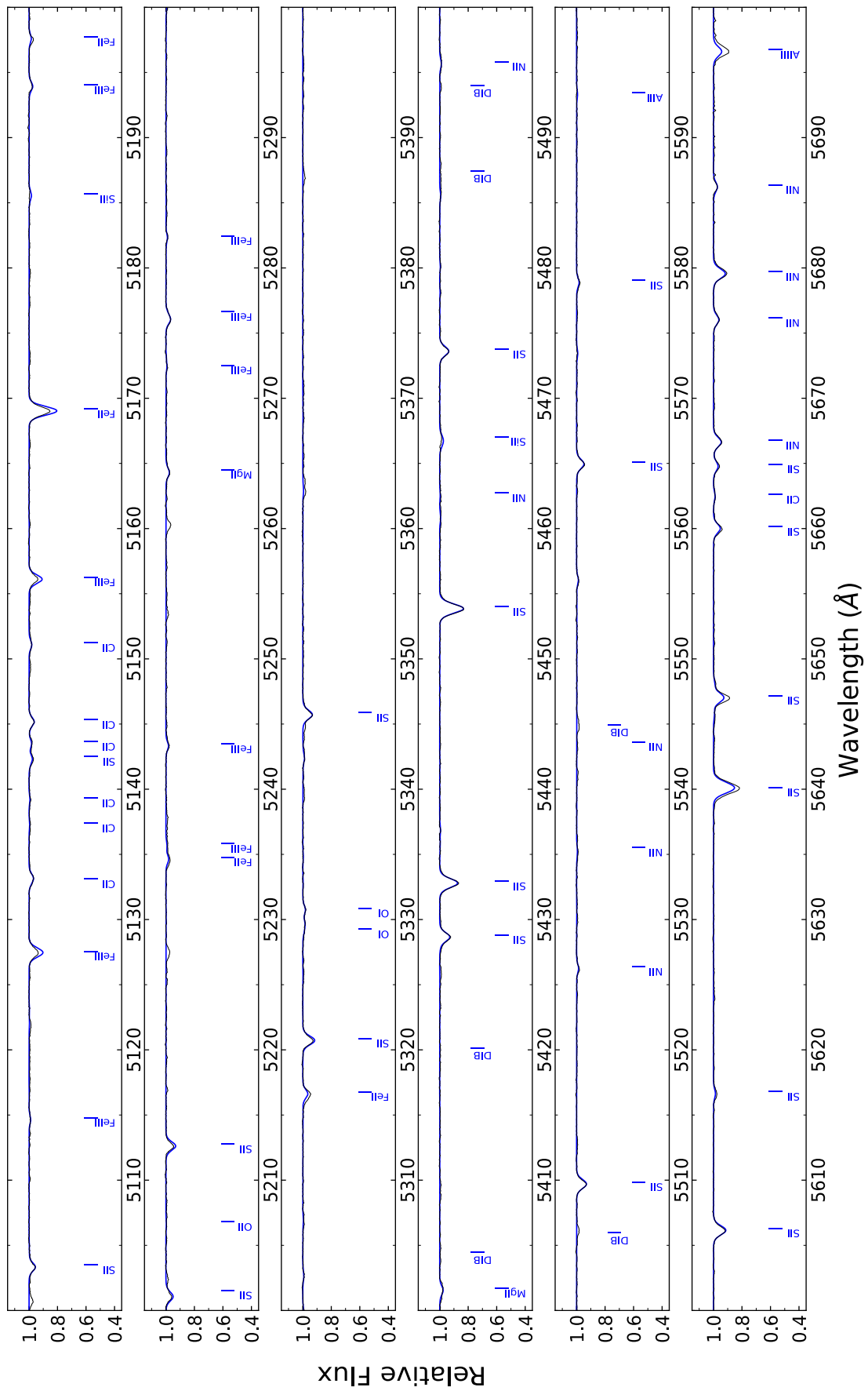


**Fig. A.3.** Same as Fig. A.1, but in the wavelength range  $\lambda\lambda 5100\text{--}5700\text{ \AA}$ .

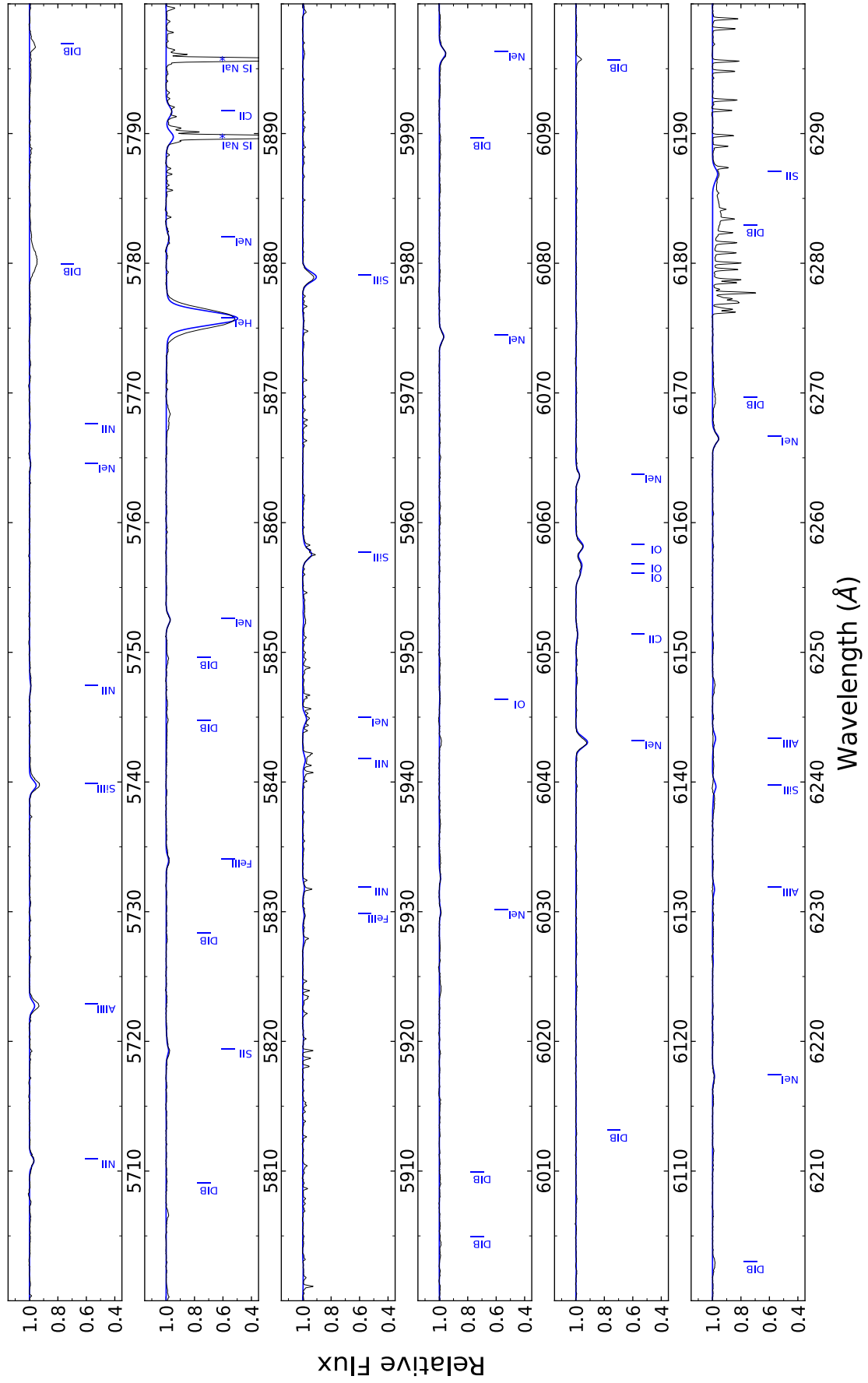


**Fig. A.4.** Same as Fig. A.1, but in the wavelength range  $\lambda\lambda 5700$ – $6300$  Å.



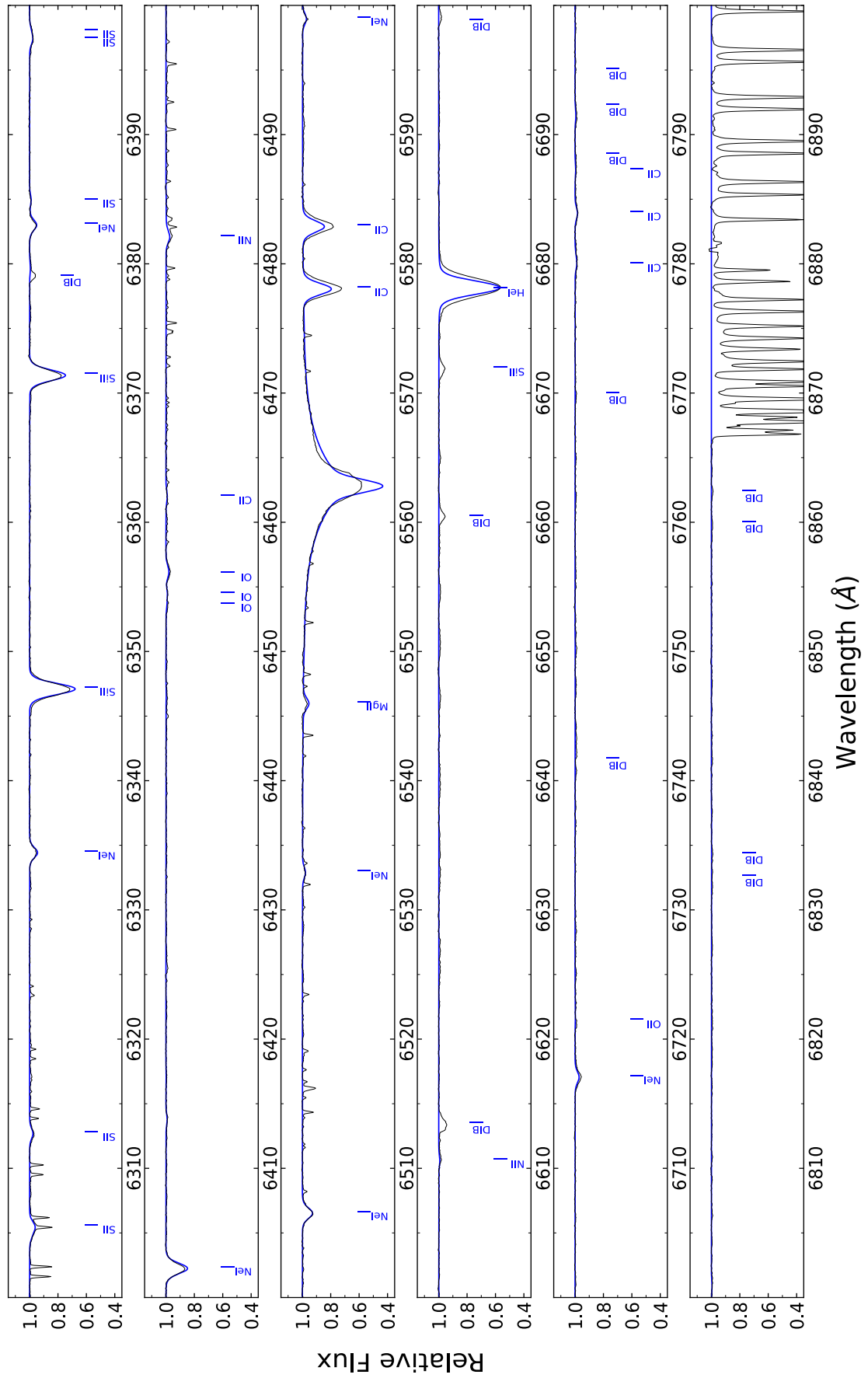


**Fig. A.5.** Same as Fig. A.1, but in the wavelength range  $\lambda\lambda 6300\text{--}6900$  Å.

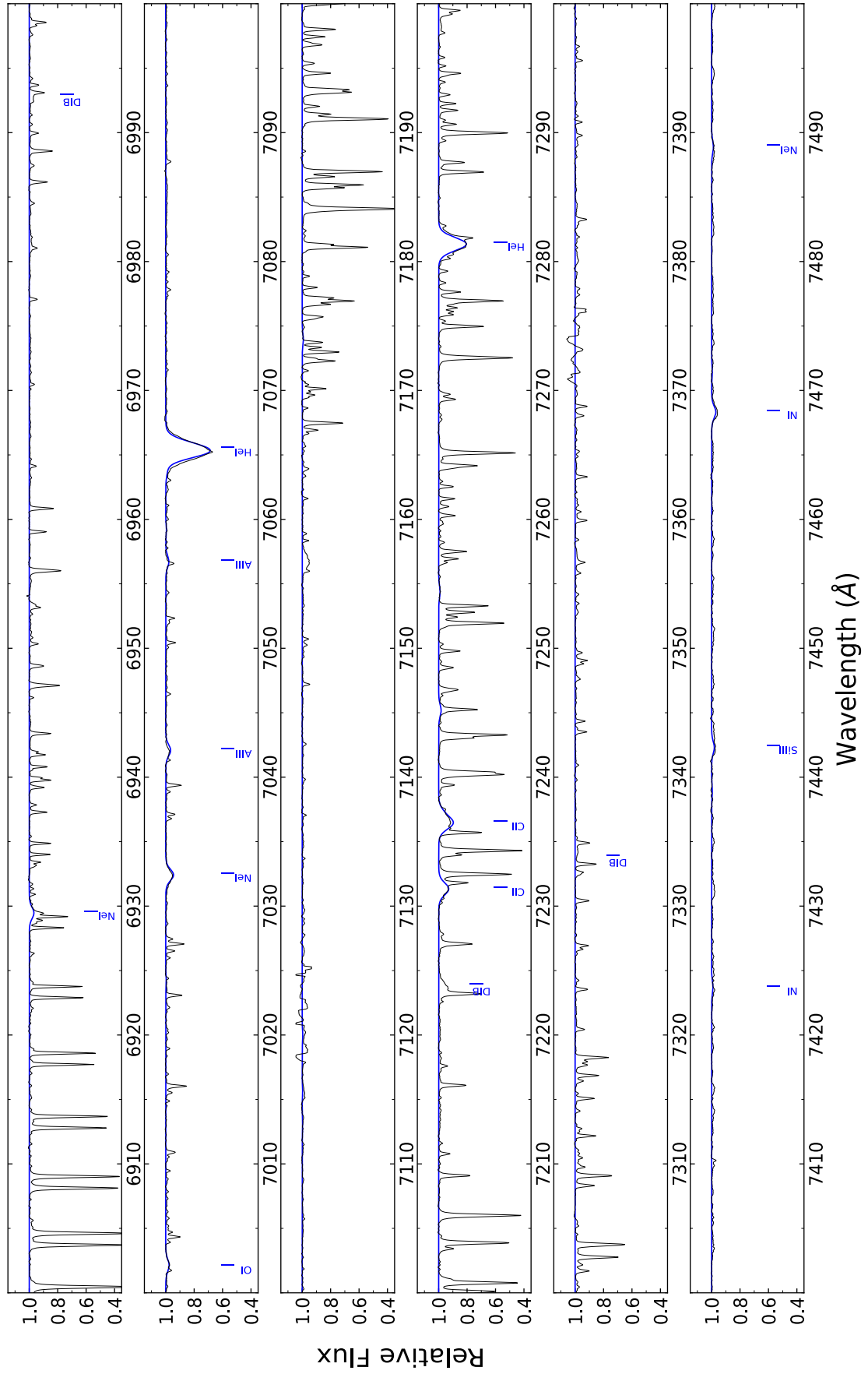


**Fig. A.6.** Same as Fig. A.1, but in the wavelength range  $\lambda\lambda 6900\text{--}7500$  Å.

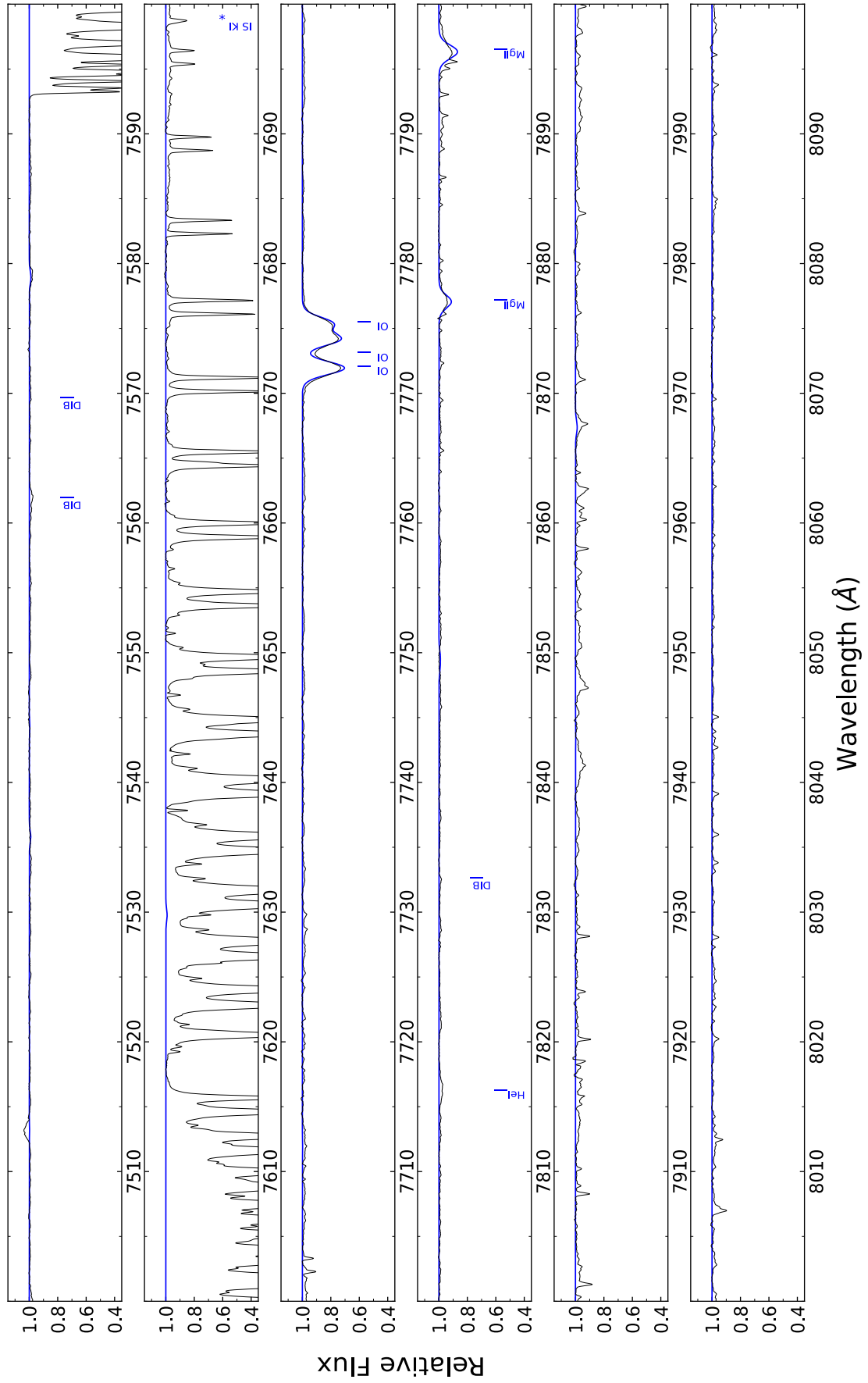


**Fig. A.7.** Same as Fig. A.1, but in the wavelength range  $\lambda\lambda 7500\text{--}8100$  Å.

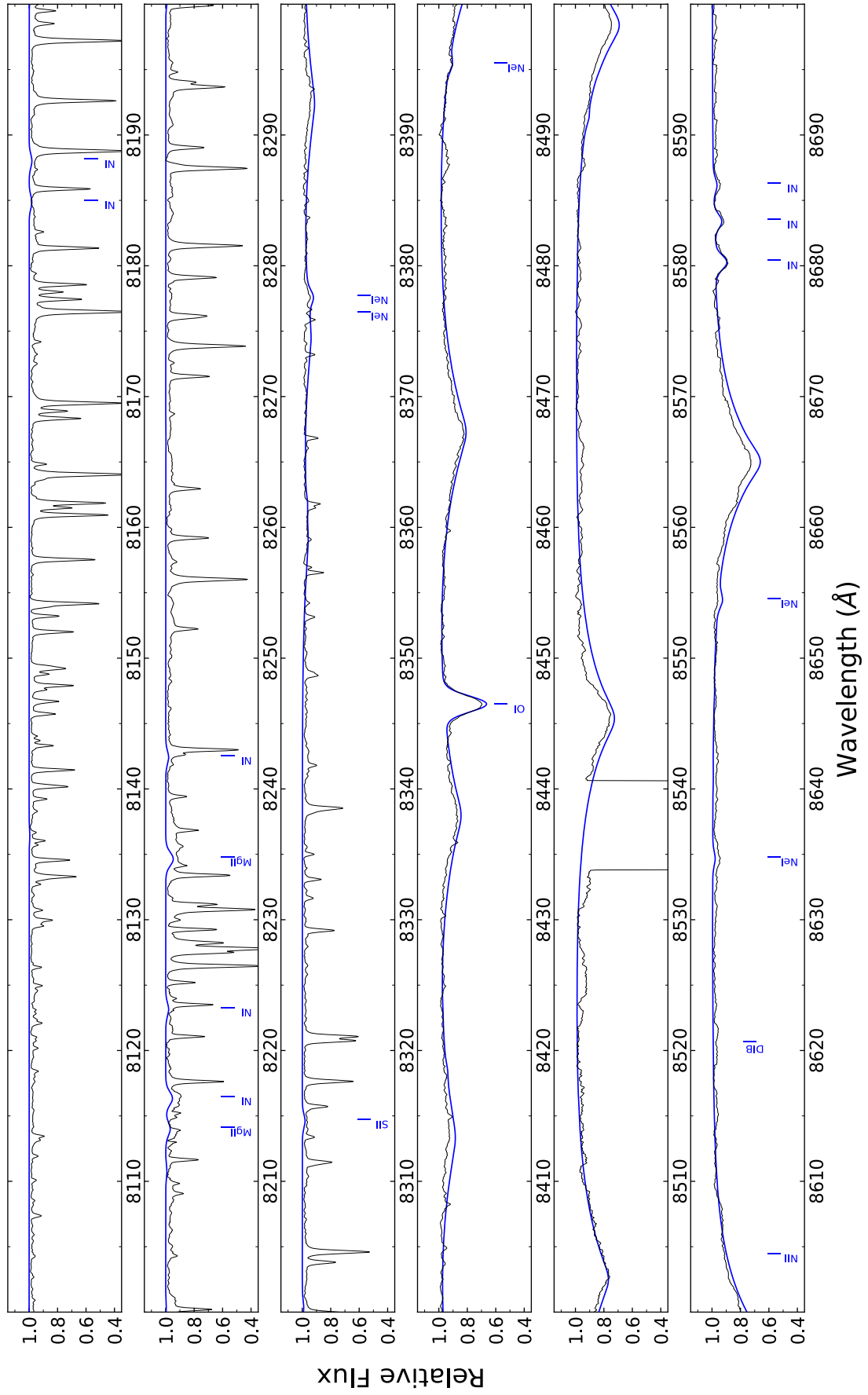


**Fig. A.8.** Same as Fig. A.1, but in the wavelength range  $\lambda\lambda 8100\text{--}8700$  Å.